Draft version July 29, 2020
Typeset using LaTeX **twocolumn** style in AASTeX62

The Ionised- and Cool-Gas Content of The BR1202-0725 System as seen by MUSE and ALMA.

A. B. Drake,[1] F. Walter,[1] M. Novak,[1] E. P. Farina,[2,1] M. Neeleman,[1] D. Riechers,[3,1] C. Carilli,[4,5] R. Decarli,[6] C. Mazzucchelli,[7] and M. Onoue[1]

[1] *Max Planck Institute für Astronomie, Königstuhl, Heidelberg, Germany*
[2] *Max Planck Institute for Astrophysics, Karl-Schwarzschild-Str, Garching, Germany*
[3] *Department of Astronomy, Cornell University, Space Sciences Building, Ithaca, NY 14853, USA*
[4] *National Radio Astronomy Observatory, Pete V. Domenici Array Science Center, P.O. Box O, Socorro, NM 87801, USA*
[5] *Cavendish Astrophysics Group, University of Cambridge, Cambridge, CB3 0HE, UK*
[6] *INAF - Osservatorio Astronomico di Bologna, Via Piero Gobetti, 93/3, 40129 Bologna BO, Italy*
[7] *European Southern Observatory, Alonso de Cordova 3107, Vitacura, Region Metropolitana, Chile*

(Accepted July 21, 2020)

Submitted to ApJ

ABSTRACT

We present MUSE observations of the gas-rich major-merger BR1202 − 0725 at $z \sim 4.7$, which constitutes one of the most overdense fields known in the early Universe. We utilise these data in conjunction with existing ALMA observations to compare and contrast the spatially resolved ionised- and cool-gas content of this system which hosts a quasar (QSO), a sub-millimeter galaxy (SMG), the two known optical companions ("LAE 1", "LAE 2"), and an additional companion discovered in this work "LAE 3" just 5″ to the North of the QSO. We find that QSO BR1202 − 0725 exhibits a large Lyα halo, covering $\approx$ 55 pkpc on-sky at surface brightness levels of SB$\geq 1 \times 10^{-17}$erg s^{-1} cm^{-2} arcsec^{-2}. In contrast, the SMG, of similar far-infrared luminosity and star formation rate (SFR), does not exhibit such a Lyα halo. The QSO's halo exhibits high velocity widths ($\sim$ 1000 km s^{-1}) but the gas motion is to some extent kinematically coupled with the previously observed [CII] bridge between the QSO and the SMG. We note that the object known in the literature as LAE 2 shows no local peak of Lyα emission, rather, its profile is more consistent with being part of the QSO's extended Lyα halo. The properties of LAE 3 are typical of high-redshift LAEs; we measure $F_{Ly\alpha}$(LAE 3) $= 0.24 \pm 0.03 \times 10^{-16}$erg s^{-1} cm^{-2}, corresponding to SFR$_{Ly\alpha} \approx 5.0 \pm 0.5$ M$_\odot$ yr^{-1}. The velocity width is Δv(LAE 3) $\approx$ 400 km s^{-1}, and equivalent width EW$_0$(Ly$\alpha\,^{lim}_{5\sigma}$) $\geq$ 34.05 Å, consistent with star formation being the primary driver of Lyα emission. We also note a coherent absorption feature at ~ -400km s^{-1} in spectra from at least three objects; the QSO, LAE 1 and "LAE 2" which could imply the presence of an expanding neutral gas shell with an extent of at least 24 pkpc.

Keywords: Quasars; BR1202; Lyα halo, LAEs, high-redshift

1. INTRODUCTION

The BR1202 − 0725 system is a prime example of a gas-rich major-merger at high redshift, which theory and simulations suggest are key to our understanding of galaxy evolution. Quasi-Stellar Object (QSO) 'BR1202 − 0725', was discovered in the *APM-BRI* survey (Irwin et al. 1991) – it was the first object at z> 4 to be detected in CO emission (Ohta et al. 1996), and these molecular gas observations revealed for the first time an optically-obscured sub-mm galaxy (SMG) lying $\sim 4''$ to the North-West of the QSO (Omont et al. 1996b, Iono et al. 2006). Subsequently, the field has been targeted with a multi-wavelength campaign of observations to measure its gas content (Wagg et al. 2012,

Corresponding author: Alyssa Drake
drake@mpia.de

Carilli et al. 2013), and chemical abundances (Decarli et al. 2017, Lehnert et al. 2020).

Indeed, the hierarchical growth of structure predicts that QSOs at high redshift are biased tracers of galaxy formation, situated in overdense environments (e.g. Overzier et al. 2009). In the case of QSO BR1202 − 0725, in addition to the nearby SMG, narrowband data have indicated the presence of two Lyman-α emitters (LAEs) in the vicinity (Hu et al. 1996, Omont et al. 1996b, Ohyama et al. 2004, Salomé et al. 2012): the source denoted LAE 1, positioned to the North-West of the QSO (in the direction of the SMG) and LAE 2 towards the South-West. Futhermore, $[\mathrm{CII}]_{158\mu\mathrm{m}}$ observations of the entire BR1202 − 0725 field from the commissioning of the Atacama Large Millimetre Array (ALMA; Wootten & Thompson 2009), suggest the possible presence of a bridge of $[\mathrm{CII}]_{158\mu\mathrm{m}}$ emission between the QSO and the SMG, tracing cooler ionised and/or neutral gas, intriguingly with an indication of a local maximum at the position of LAE 1. Together, this makes BR1202 − 0725 an ideal system to study a diverse population of galaxies evolving in one of the most overdense regions of the Universe known, just ~ 1.2 Gyr after the Big Bang.

The nature of the two companion objects denoted LAE 1 and LAE 2 has been debated. The object that appears in HST775W and HST814W imaging, later named LAE 1, was spectroscopically confirmed by the detection of Lyα emission in Hu et al. (1996). The optical line ratios presented in Williams et al. (2014) suggest that the primary source of Lyα emission in LAE 1 is star formation i.e. neither CIV nor HeII emission is detected, which should each be present in the case of photoionisation by an active galactic nucleus (AGN)[1]. LAE 1 is detected in $[\mathrm{CII}]_{158\mu\mathrm{m}}$ (Carilli et al. 2013, Wagg et al. 2012), and shows a narrow emission line (of width $\Delta v_{[\mathrm{CII}]} = 56$ km s^{-1} at full width half-maximum; FWHM), taking this as an indicator of systemic redshift, the Lyα emission is offset by 49 km s^{-1} from its predicted position in wavelength (Williams et al. 2014). Observations in Decarli et al. (2017), Pavesi et al. (2016), and Lee et al. (2019) detect $[\mathrm{NII}]_{122\mu\mathrm{m}}$ emission from ionised Nitrogen at the position of LAE 1, at levels which suggest an origin within HII regions.

LAE 2 (Hu et al. 1997, Salomé et al. 2012), appears in narrowband imaging to be an LAE at the redshift of the QSO. Long-slit spectroscopic observations in Williams et al. (2014) confirmed the presence of Lyα emission at the position of LAE 2, at approximately the redshift of the QSO, lending support to the idea that the object was indeed an LAE associasted with this group. The [CII] emission from LAE 2 falls at the edge of the ALMA spectral setup, and hence it is not easy to judge the peak frequency or velocity width of the line (see Carilli et al. 2013 and Wagg et al. 2012). Decarli et al. (2017) however reported an [NII]/[CII] ratio for this object, which indicated that this sub-mm emission in LAE 2 is likely to originate from HII dominated regions, and as such the object could be forming stars.

In addition to the presence of companion galaxies at the redshift of the QSO, these massive objects are predicted to reside at the nodes of large-scale structure, composed of sheets and filaments of HI gas, known as the 'cosmic web' (e.g. Springel et al. 2006). This gas is too diffuse to form stars, but instead is funnelled along the filamentary structure onto massive dark-matter halos hosting the QSO and/or other massive collapsed objects (e.g. van de Voort et al. 2011), acting as fuel for their star formation. As a QSO is 'fed' by this cool gas ($T \sim 10^4$ K), a number of physical processes (whose relative contributions are debated) lead to the emission of Lyα photons which, due to their resonant nature in HI gas, require careful interpretation, including modelling of their complex radiative transfer processes (e.g. Michel-Dansac et al. 2020). Although extended Lyα halos can arise surrounding a diverse set of objects (e.g. Venemans et al. 2007) in the case of a central QSO, the prime candidates responsible for powering the Lyα emission could be any of the following; (A) Photoionisation of the cool gas by a centrally located AGN (sometimes referred to as 'Lyα fluorescence'; Cantalupo 2010, Prescott et al. 2015); (B) 'gravitational cooling' of in-flowing (pristine) gas, in which collisional excitation of atoms is the dominant power source (Smith & Jarvis 2007; Rosdahl & Blaizot 2012; Daddi et al. 2020); and (C) shock-heating of the gas as a result of violent, possibly jet-induced star formation (e.g. Taniguchi et al. 2001). In addition to these processes, star formation within the QSO's host galaxy, and/or star formation within other satellite galaxies could act as energy sources to also photoionise some fraction of the cool gas.

In recent years, observations from the panoramic integral field spectrograph MUSE (Bacon et al. 2010) have revolutionised the field of study surrounding the detection and analysis of extended Lyα halos/nebulae around QSOs and 'normal' star-forming galaxies (Bacon et al. 2015, Wisotzki et al. 2016, Bacon et al. 2017, Inami et al. 2017, Drake et al. 2017a, Drake et al. 2017b,

[1] Although CIV could be suppressed in a low metallicity system, HeII should be detectable regardless, and thus places a strong constraint on the powering mechanism of the Lyα emission.

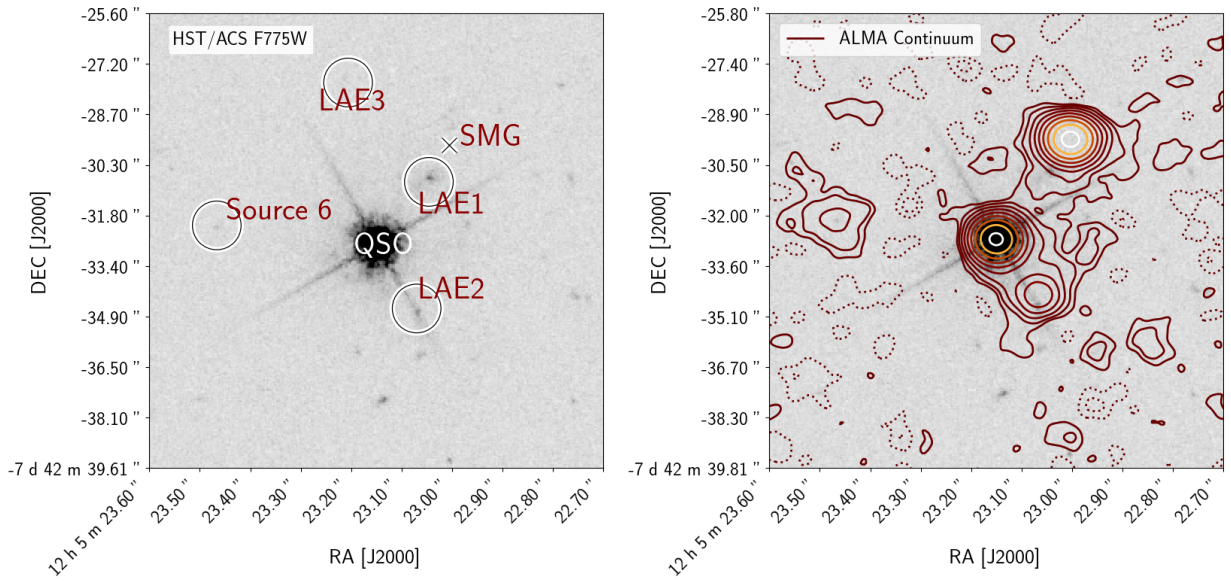

Figure 1. HST775W imaging is displayed in both panels, providing the highest resolution optical data available for the field. In the left-hand panel we highlight the positions of the QSO, the (optically-obscured) SMG, two known objects dubbed LAE 1 and LAE 2; a previously unreported source that we present in this work; LAE 3, and another previously unreported source which we name Source 6; hereafter "SRC 6". In the right-hand panel we display the same HST image, this time overlaid with sub-mm continuum contours from ALMA. Contours are linearly spaced at $\pm$ 1.5, 3.0, 6.0, 12.0, 24.0, 48.0, 96.0, 192.0 and 384.0 σ where $1\sigma = 12.38\ \mu\mathrm{Jy\,beam^{-1}}$, and negative contours are represented by dotted lines. The presence of the QSO and the optically-obscured SMG are both demonstrated at $>15\,\sigma$, with emission of lower-significance present surrounding the positions of LAE 1, LAE 2, and SRC 6.

Leclercq et al. 2017). The high spectral ($\Delta\lambda$ = 1.25 Å) and spatial (0.202″) resolution have revealed detailed spatially-resolved kinematic maps of Lyα halos surrounding QSOs at the highest redshifts (Farina et al. 2017, Ginolfi et al. 2018, Drake et al. 2019, Farina et al. 2019), and at z$\sim$2-3 where other rest-frame ultraviolet emission lines are accessible with MUSE e.g. CIV and/or HeII potentially enabling constraints on the powering mechanisms of the halos (Arrigoni Battaia et al. 2015b, Arrigoni Battaia et al. 2015a, Borisova et al. 2016, Arrigoni Battaia et al. 2019, Marino et al. 2019; Also see results from the Keck Cosmic Web Imager e.g. Cai et al. 2019).

Until now, observations of BR1202 − 0725's ionised gas content, traced by Lyα emission, have been limited to photometry from broad or narrow-bands, long-slit spectroscopy, and early IFU observations from TIGER Petitjean et al. (1996). In this paper we present IFU data covering the BR1202 − 0725 field from MUSE – simultaneously revealing an extended Lyα halo around the QSO, allowing the re-analysis of Lyα emission from companion galaxies embedded within the halo, and comparing the ionised- and cool-gas properties of both Lyα halo and companion objects in the field.

This paper proceeds as follows; in Section 2 we describe the data used in this paper, and its processing before analysis. The data consist of archival HST imaging, an archival ALMA [CII] datacube, deep ALMA dust continuum imaging, and finally the MUSE datacube. We also describe briefly here our method for PSF-subtraction in the MUSE cube. In Section 3 we present MUSE images of the field, and a spectrum of the QSO, followed by the results of our PSF-subtraction. Here we analyse the spatial extent and morphology of the Lyα halo, and take advantage of the spatial resolution of MUSE to produce moment maps of the Lyα emission, and search for overlap or coincidence of Lyα and [CII] emission across the field. We speculate on the dominant powering mechanism of the Lyα halo and perform a search for extended CIV emission. Next, in Section 4 we present images and spectra of a series of companions in the field, including the SMG, LAE 1 and LAE 2. For each object in the system we assess the Lyα emission and derive velocity widths, star-formation rates (SFRs; where appropriate) and constraints on the rest-frame equivalent widths of Lyα (EW_0; again where possible) before using these measurements to re-assess the nature of the proposed companions. We summarise our findings on the QSO's Lyα halo and all accompanying objects in Section 5.

We assume a ΛCDM cosmology with $\Omega_m = 0.3$, $\Omega_\Lambda = 0.7$ and $H_0 = 70$ km s^{-1} Mpc^{-1}. In this cosmology, 1″ = 6.64 pkpc at z ≈ 4.69.

2. OBSERVATIONS AND DATA REDUCTION

In addition to our analysis of the new MUSE observations, we make use of two existing datasets from ALMA; allowing a multiwavelength comparison of the ionised and neutral gas content of the BR1202 − 0725 system; and archival HST imaging to give an optical overview of the field at the highest-resolution available. The datasets are described below.

2.1. *HST overview of the field*

In Figure 1 we show the archival HST775W image of BR1202 − 0725 highlighting in the left panel the positions of the QSO, the SMG, two known-LAEs (LAE 1, LAE 2) and an additional LAE discovered in this work; LAE 3. In the right-hand panel we show the HST775W image again, overlaying sub-mm dust continuum contours from the deepest ALMA observations of the field, see Section 2.2.1 for a description. Both the archival HST imaging, and the dust-continuum maps are used throughout this work for orientation purposes only.

2.2. *ALMA Observations*

2.2.1. *Deep Continuum Imaging*

In order to obtain a deep mm continuum map we explored all public data in the ALMA archive available for our system. Projected baseline lengths for the combined continuum dataset are between 14 - 1440 m, with the 80th percentile at 288 m. We decided to combine the data in the frequency range of 190 – 297 GHz (bands 5, 6 and 7). Inside this 107 GHz bandwidth, 33 GHz was observed with six frequency setups[2]. These setups cover several far-infrared (FIR) bright molecular emission lines of CO (high excitation rotational CO lines $J_{up} = 10$, 12, 14) and H_2O, and a fine atomic transition line [NII] at 205 microns. A total width of 1500 km s^{-1} centered at each of the emission lines was excluded from the continuum imaging process. This width choice corresponds to two times the FWHM of the brightest [CII] line detected in the SMG inside this system Carilli et al. (2013). The continuum map was obtained from the remaining line-free channels spanning an effective bandwidth of 25 GHz. Individual spectral setups were observed at roughly similar resolutions, with synthesized beam FWHM range of 0.6″- 1.5″, and a position angle of 88°, thus allowing joint imaging of all the datasets. For imaging we use the TCLEAN task contained in the Common Astronomy Software Applications (CASA[3]) package (McMullin et al. 2007). Given the large bandwidth available, we image the data using the multi-term multi-frequency synthesis (MTMFS, NTERMS=2, Rau & Cornwell 2011). The data were imaged with natural weighting to maximize the point source sensitivity. The synthesised beam side-lobes of the combined dataset are smaller than 5%. Due to good quality of the final map, no additional weighting of visibilities was deemed necessary[4]. Cleaning was performed with the multi-scales algorithm (using scales corresponding to a single pixel, 1x, and 3x the beam size) first down to 5σ in the entire map, and then further down to 1.5σ inside manually defined cleaning regions, which outline the observed emission. The final continuum map is given at the monochromatic frequency of 243.5 GHz, resolution of 0.83″×0.73″, and has a root-mean-square (rms) noise level of $1\sigma = 12.38$ μJy beam^{-1}.

2.2.2. *Archival [CII] Observations*

We make use of ALMA 335 GHz (Band 7) Science Verification data with a central frequency targeting the [CII] line at the redshift of the QSO and the SMG. The data were first presented in Wagg et al. (2012) and Carilli et al. (2013). We applied a velocity-frame correction to the published data to convert from the observed frame (topocentric) to the local standard of rest (LSRK) for accurate comparison to velocities in the MUSE datacube.

2.3. *MUSE Observations*

2.3.1. *MUSE Data Reduction*

MUSE data were taken as part of ESO programme 0102.A − 0428(A), PI Farina, and reduced as in Farina et al. (2017) and Farina et al. (2019) using the MUSE Data Reduction Software version 2.6 (Weilbacher et al. 2012, Weilbacher et al. 2014). Two exposures of 1426 s were taken, with < 5″ shifts and 90 degree rotations. The PSF has a size of 0.6″ at the observed wavelengths of the Lyα line (the median delivered PSF on stars in the field is closer to 0.7″). The 5σ surface brightness detection limit is 4.2×10^{-17} erg s^{-1} cm^{-2} arcsec^{-2} for an aperture of 1 square arcsecond. Data have been corrected for galactic extinction, and emission from night

[2] Few band 6 setups partially overlap.

[3] CASA version 5.4.0-70

[4] We have checked that re-weighing of combined visibilities using the STATWT task in CASA does not further improve the map quality.

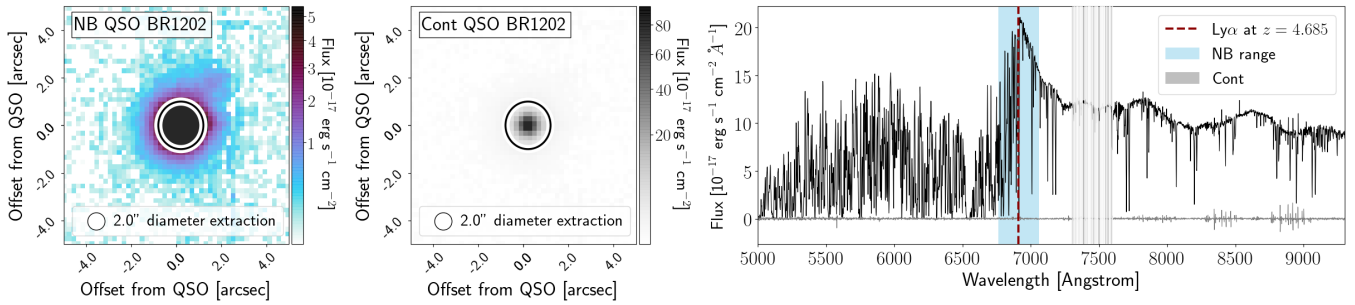

Figure 2. MUSE images and spectra of QSO BR1202 − 0725. The left-hand panel shows a fixed-width narrow-band image of $\Delta\lambda = 120$ Å centred on the predicted wavelength of Lyα according to the QSO's [CII] redshift from ALMA. The wavelength range of the narrow-band image is highlighted in orange on the spectrum to the right. In the central panel we show the PSF image (see text for details) with the spectral layers used to construct the image highlighted in pink on the spectrum. In the final column, we show the QSO spectrum extracted in an aperture of 2 arcseconds in diameter, the extraction region is given by the black circle on the narrow-band and PSF images. A dashed red line on the spectrum gives the predicted peak wavelength of the Lyα emission according to the systemic redshift of the QSO.

sky lines is removed using the Zurich Atmospheric Purge software (ZAP; Soto et al. 2016).

2.3.2. *MUSE PSF Subtraction*

With a view to uncovering low-surface-brightness Lyα emission in the MUSE data surrounding QSO BR1202 − 0725, we follow the same procedure as in Drake et al. (2019) to model and subtract the point-spread function (PSF) in the data (also demonstrated in Farina et al. 2019). In brief, this entails collapsing several spectral layers of the QSO's optical continuum which is dominated by light from the accretion disk of the AGN, and appears as a point source at the resolution of MUSE. By using the quasar itself to create the "PSF image" we avoid issues of spatial PSF-variation/interpolation across the field. The wavelength layers chosen to construct the PSF image are highlighted in pink in the right-hand panel of Figure 2. We then work systematically through the MUSE cube, scaling our PSF image such that the flux in the pixel at the image peak becomes equal to the flux of the QSO in the same spatial pixel. By subtracting this scaled PSF image from each wavelength layer we produce an entire PSF-subtracted datacube. Finally, as in Drake et al. (2019), we mask an ellipse on every layer of the datacube of radii equal to the FWHM of a 2-dimensional Gaussian fit to the PSF image, and exclude this region from further analysis to avoid residuals near the bright central source, unless otherwise noted.

3. EXTENDED LYα IN THE BR1202 − 0725 FIELD

3.1. *Total Flux of Lyα Halo around QSO BR1202 − 0725*

In Figure 3 we show a narrow-band image comprised of all the Lyα emission in a square 12″ region surrounding the QSO. The narrowband width was chosen to encompass the entirety of the red side of the Lyα line after PSF-subtraction, and to include emission out to the same velocity bluewards of the systemic redshift of the QSO. This amounts to a total of 61Å, or $\approx$ 2640 km s^{-1}. In the right-hand panel of Figure 3 we show the PSF-subtracted spectrum extracted in a 3″ diameter aperture shaded in blue, and over plot with a black line the PSF-subtracted spectrum that results from summing all emission within the 1×10^{-17} erg s^{-1} cm^{-2} arcsec^{-2} surface-brightness contour. Interestingly the halo's spectral shape is somewhat 'flat-topped', which may be the result of contributions from objects at different velocities within the halo, or simply represent an intrinsically broad line. The flux of diffuse Lyα within the SB$= 1 \times 10^{-17}$ erg s^{-1} cm^{-2} arcsec^{-2} surface-brightness contour is $F_{Ly\alpha} = 1.39 \pm 0.01 \times 10^{-15}$ erg s^{-1} cm^{-2}, after continuum-subtraction, masking both the position of the QSO (across a 1″ diameter), and LAE 1 (across a 1.6″ diameter). If the halo emission were powered solely by star formation, we could translate this to an SFR according to Equation 1 (Ouchi et al. 2003):

$$SFR_{Ly\alpha}(M_{\odot} yr^{-1}) = L_{Ly\alpha} \times 1.05 \times 10^{42.0} \mathrm{erg\,s^{-1}} \quad (1)$$

where $L_{Ly\alpha}$ is the Lyα luminosity in cgs units. Our measured flux translates to a luminosity of $L_{Ly\alpha} = 3.11 \times 10^{44}$ erg s^{-1}, which would then correspond to an SFR of almost ≈ 300 M$_{\odot}$ yr^{-1}.

3.2. *Morphology of Extended Lyα around QSO BR1202 − 0725*

To examine the distribution of the diffuse Lyα in more detail, we show in Figure 4 a narrow velocity range ($\sim$ 200 km s^{-1}; i.e. a collapse of the monochro-

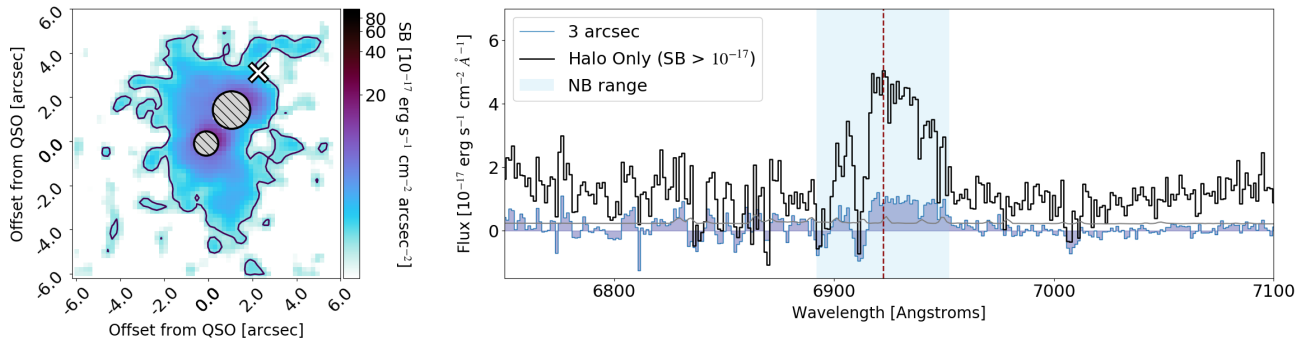

Figure 3. A smoothed surface brightness image and spectrum of the continuum- and PSF-subtracted Lyα halo surrounding the QSO. In the left-hand panel we show a narrow-band image smoothed with a Gaussian kernel of $\sigma = 1$ pixel, in units of surface brightness. A single contour is displayed at SB= 1×10^{-17} erg s^{-1} cm^{-2} arcsec^{-2} (black line). The QSO position is masked over a diameter of 1″, and LAE 1 is masked over a diameter of 1.6″, we also mark the position of the SMG on this image with a white cross. In the right-hand panel we show in filled-blue the spectrum extracted from the continuum- and PSF-subtracted cube within a 3″ diameter aperture (after employing the mask for residuals), and overlay in black a spectrum extracted by summing all the voxels (volumetric pixels) lying within the 1×10^{-17} erg s^{-1} cm^{-2} arcsec^{-2} contour with the QSO and the position of LAE 1 masked. The dashed red line gives the predicted position of the peak of the Lyα emission according to the systemic redshift of the QSO (Table 1), the shaded orange region corresponds to the wavelength region that makes up the narrow-band image, and we also overplot in red the sky spectrum.

Table 1. Known objects in the BR1202 system at the time of writing. The first column gives the literature redshift oftheobject. The second column gives the offset in velocity between this object and the QSO. The third column gives the predicted wavelength of Lyα emission given the systemic redshift of the object. In the final column we include notes on each object.

Object	$z_{[\rm CII]}$[a]	**Vel Offset**[b] [kms^{-1}]	**Pred λ Lyα** [Å]	**References**
QSO	4.6942	0.0	6922.27	McMahon et al. (1994), Isaak et al. (1994)
SMG	4.6915	-142.1	6918.99	Omont et al. (1996a), Riechers et al. (2006)
LAE 1	4.6950	42.0	6923.24	Hu et al. (1996), Ohyama et al. (2004)
LAE 2	4.7055	595.5	6936.01	Hu et al. (1997), Wagg et al. (2012), Carilli et al. (2013)

[a]Carilli et al. (2013), formal errors from Gaussian fitting on the redshifts are each <0.0003.
[b]Object's velocity offset from the QSO, where negative numbers represent a blue-shift, and positive numbers a red-shift.

matic wavelength layers between 6927 and 6932 Å). This choice of velocity range reveals filamentary structure at low surface-brightness levels, highlighting the complex morphology of the halo, while encompassing wavelength layers within which the QSO, LAE 1, LAE 2 and LAE 3 are all visible. In the top left-hand panel we show the Lyα surface brightness, contoured between SB= 5×10^{-19} and 5×10^{-18} erg s^{-1} cm^{-2} arcsec^{-2}, and again highlight the positions of the QSO, the SMG, and three LAEs in the system. Figure 4 demonstrates that diffuse Lyα connects all three objects, while none is seen surrounding the SMG. Interestingly, the low-surface-brightness emission in Lyα extends directly in the direction of the optically-obscured SMG, and fully encompasses the position of LAE 1, however by the position of the SMG, the halo is no longer visible in this velocity range. The Lyα emission at the position of LAE 2 however appears indistinguishable from the halo extending from the QSO in this image – we return to this in Section 4.2. Finally, LAE 3 appears as a distinct source in Lyα, however its emission is possibly connected via a low-surface-brightness bridge of Lyα emission to the position of the QSO. In the top right-hand panel we display the same Lyα surface-brightness image, but this time overlay contours depicting [CII] emission (Wagg et al. 2012 and Carilli et al. 2013) from the entire collapsed data cube. In the lower panels, we show cutouts at three different velocites relative to the systemic redshift of QSO BR1202 − 0725 (i.e. a velocity slice of the Lyα halo overlaid with contours depicting [CII] emission in the corresponding velocity slice). The velocities shown here were selected from the full series of channel maps presented in Appendix B, and are chosen to highlight a number of features. First, the purported [CII] bridge between the QSO and the SMG. This is seen at negative velocities (which correspond to the slightly lower redshift of the SMG than the QSO) which is seen across multiple channels. Secondly, in the central panel we

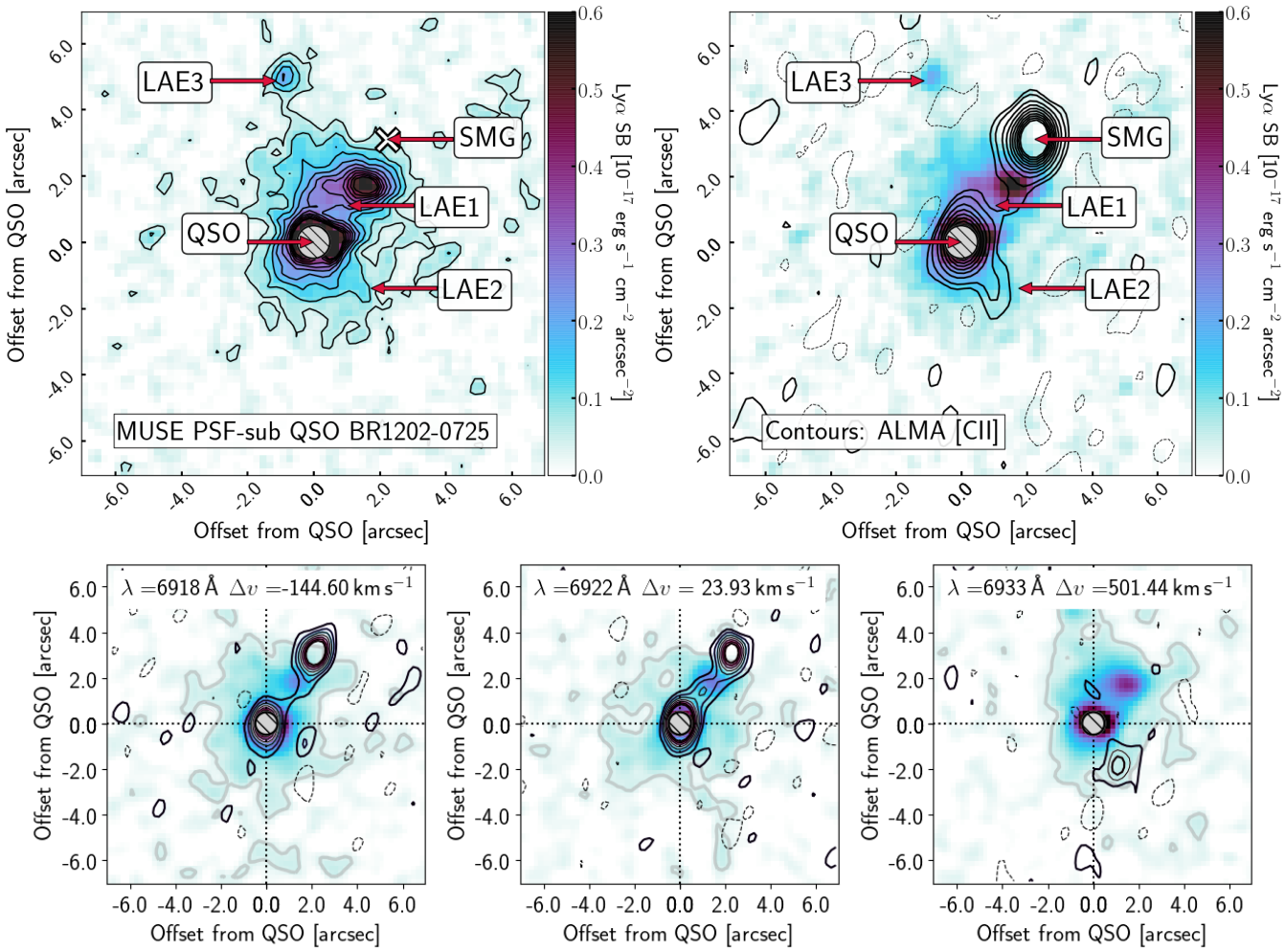

Figure 4. PSF-subtracted narrow-band MUSE images centred on the Lyα line are displayed together with contours to depict either the significance of the Lyα emission or the coincident [CII] emission. In the upper panels the MUSE image is a collapse of the monochromatic wavelength layers between 6927 and 6932 Å; i.e. a narrow velocity range ($\sim$ 200 km s^{-1}) in surface brightness units (erg s^{-1} cm^{-2} arcsec^{-2}). In the left-hand panel we overlay contours ranging between 5×10^{-19} and 5×10^{-18} erg s^{-1} cm^{-2} arcsec^{-2} denoting the Lyα surface brightness. In the right-hand panel we instead overlay linearly-spaced contours denoting [CII] emission from archival ALMA observations across the entire velocity range of the data cube. Contours are linearly spaced at $\pm$ 1.5, 3.0, 6.0, 9.0, 12.0 and 15.0 σ, and negative contours are represented by dotted lines. In both panels residuals from PSF subtraction are masked across 1″ at the position of the QSO. In the lower three panels we show cutouts at specific velocities of Lyα and [CII] emission taken from the full set of channel maps presented in Appendix B. In these panels we include a single grey contour to depict the 0.5 σ level of the extended Lyα, and overlay linearly-spaced contours denoting [CII] emission beginning at 2σ.

show the channel closest to systemic, the extended [CII] persists, with a local maximum thought to define the position of LAE 1's ISM. In the final panel, 500 km s^{-1} red-ward of the QSO, the position of LAE 2 becomes clear. Together, these data begin to highlight the diversity of properties of the objects in this field. While the QSO appears bright in both Lyα and [CII] emission, the SMG appears only at sub-mm wavelengths. LAEs 1 and 2 show [CII] emission most visible in channels at their respective velocities, however LAE 3 does not show any associated [CII] emission. We will return to each of these features and discuss the objects' nature in Section 4.

3.3. *Kinematic analysis of Lyα around QSO BR1202 − 0725*

To analyse the internal kinematics of the extended Lyα emission, we present zeroth-, first- and second-moment maps (representing the total flux, velocity and dispersion maps, respectively) in Figure 5, relative to the predicted peak of the Lyα line at a systemic redshift of $z = 4.6942$. We analyse the data in a manner consistent with Drake et al. (2019); we first smooth the

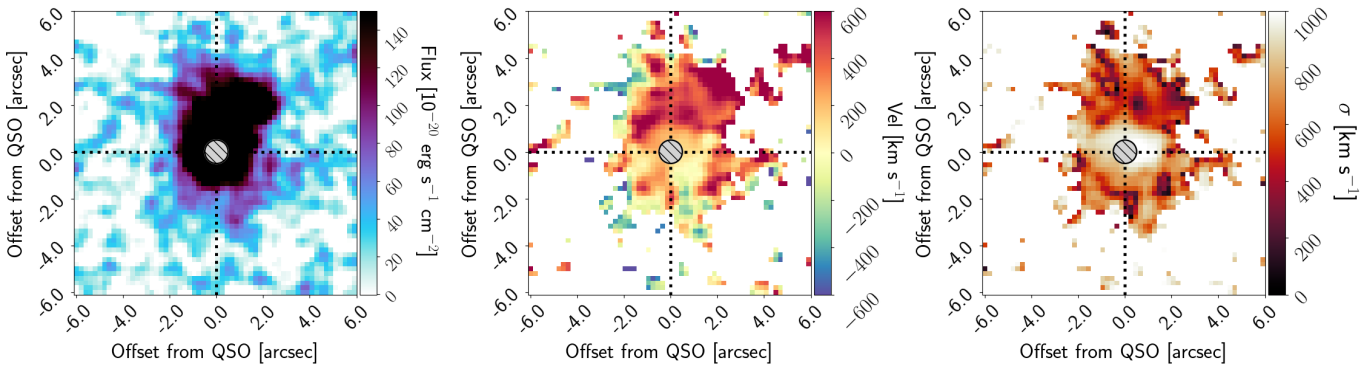

Figure 5. Lyα moment maps for the PSF-subtracted Lyα halo around QSO BR1202 − 0725. The left-hand panel shows moment zero (a flux image) containing all volumetric pixels, that make up the rest of the kinematic analysis. The moment analysis is performed across the wavelength range 6882 − 6962 Å- i.e. approximately the same range shown in Figure 3. In the central panel we show the first moment, i.e. the velocity of each spatial pixel relative to the peak of the halo Lyα emission, and in the right-hand panel we show the second moment, or velocity dispersion in each spatial pixel. Residuals from the PSF subtraction are masked across 1″ around the QSO in each panel.

datacube in the two spatial directions with a Gaussian kernel of $\sigma = 1.0$ pixel, and calculate the non-parametric moments of the data, i.e. we do not assume any functional form for the Lyα spectral shape. In the first panel we show the flux-weighted zeroth-moment. This image/map is essentially the same as that shown on the left-hand side of Figure 3.

In the central panel we show the first moment of the halo's Lyα emission, which gives the flux-weighted velocity of the halo gas relative to the peak of the emission, applying a uniform post-processing S/N cut of 1.0 on the moment zero image. The velocity structure is clumpy and complex. The majority of the extended emission, which appears to the North of the QSO, is red-shifted by a few hundred km s^{-1}, only small patches of emission ($\leq 2''$ on-sky) appear blue-shifted, and they each appear towards the South of QSO. LAE 1 does not appear kinematically distinct from the halo. No obvious signs of a flow of gas between the two objects is seen in this map, however for a more thorough examination of the relative velocities of Lyα and [CII] emission across the field of view we refer the reader to Appendix B where we show a series of 'channel maps', displaying images of the extended Lyα emission seen with MUSE, overlaid with [CII] contours from ALMA (see Carilli et al. 2013 and Wagg et al. 2012). The spectral resolution of MUSE at ~ 7000Å corresponds to $\sim \Delta v = 100$ kms^{-1}. The channel spacing in velocity of the [CII] emission seen with ALMA, is $\sim \Delta v = 35$ km s^{-1}. The maps show that the extended Lyα emission is to some extent co-spatial with the [CII], and peaks at the same velocities as the [CII] bridge between BR1202 − 0725 and the SMG proposed in Carilli et al. (2013). The Lyα emission is however much broader than the [CII], and as such Lyα still appears bright in channels beyond the end of the ALMA [CII] coverage.

Finally, in the third panel of Figure 5, we show the second moment, σ, giving the velocity dispersion of the gas, and applying the same uniform S/N cut of 1.0 on the moment zero image. Velocities close-in to the QSO are very high, of order ~ 1000 km s^{-1}, with a region of lower values (of order 500 km s^{-1}) in the direction of LAE 1.

3.4. *Constraints on the dynamical mass of the halo*

Using the moment maps, we can roughly estimate the dynamical mass of this gas given a number of assumptions. For instance, in the moment zero flux image (Figure 5, left) where the entire width of the Lyα line is collapsed, emission stretches $\approx 8''$ North−South, and $\approx 8''$ East−West surrounding the QSO. We therefore take an average radius of $4''$, which corresponds to ≈ 27 pkpc at $z = 4.69$. In the moment 1 map (Figure 5, centre) we see a gradient of approximately $v \approx \pm 300$ km s^{-1} across the halo. Then, if one assumes rotation of the gas is responsible for the velocity gradient, we solve for dynamical mass $M_{\rm dyn}$:

$$M_{\rm dyn} = rv^2/G \qquad (2)$$

where G is the gravitational constant, r is the halo radius, and v is the velocity range across this radius. As we have no information on inclination angle, we place a lower limit on the dynamical mass of the halo; $M_{\rm dyn} \geq 6 \times 10^{11}$ M$_\odot$. Even without any correction for inclination angle, this is significantly larger than the

combined molecular gas mass of the QSO-SMG system reported in the literature ($\sim 10^{11}$ $M_\odot$; Omont et al. 1996a, Riechers et al. 2006), and 2 orders of magnitude larger than the QSO's black hole mass, $M_{BH} = 1.9 \times 10^9$ $M_\odot$ (Carniani et al. 2013).

3.5. *Speculation on Lyα powering mechanism*

The powering mechanisms of Lyα halos at high redshift have long been debated. BR1202 − 0725 is an example of a system where any one of the proposed mechanisms outlined in Section 1 could naively be assumed the primary driver of the halo emission, or perhaps more likely, a complex mixture of processes are responsible. The QSO has an obscured star-formation rate in excess of 1000 $M_\odot\,yr^{-1}$ (Carilli et al. 2013), and as such, in-situ star-formation could be responsible for the extended Lyα emission. Likewise, copious amounts of pristine gas are required to fuel this major merger which could give rise to gravitational cooling of the gas as it is funnelled onto the QSO. It is perhaps of some significance then that QSO BR1202 − 0725 is accompanied by the SMG of similar gas mass, inferred SFR, and dust content (Carilli et al. 2013), but that displays no prominant Lyα halo. In the absence of any further diagnostics, this lends support to the idea that the Lyα halo is directly linked to the actively accreting SMBH in the QSO, and not to star formation.

Several studies in the literature have recently taken steps towards identifying the powering mechanisms of Lyα halos around QSOs through the use of additional diagnostic lines (Arrigoni Battaia et al. 2018). Motivated by these studies, we take advantage of the spectral coverage of MUSE to search for any extended CIV emission surrounding BR1202 − 0725. The metal line CIV indicates whether the Lyα emitting gas has been enriched (i.e. it orignated within the host galaxy) or is pristine (falling onto the halo for the first time). In Appendix C we show the MUSE spectrum of QSO BR1202 − 0725 again, and overlay a composite quasar spectrum (Selsing et al. 2016), 'red-shifted' to $z = 4.6942$. We highlight on this spectrum the predicted observed wavelengths of various emission lines, in particular CIV $\lambda_{em} = 1549$Å. We extract an image and spectrum exactly as for Lyα in Figure 3, but this time centred on the predicted wavlength of CIV. We detect no extended CIV emission down to a surface brightness limit of 0.19×10^{-16} $erg\,s^{-1}\,cm^{-2}\,arcsec^{-2}$ in a square arcsecond. Given however that metal lines in high-redshift QSOs are frequently observed to be blueshifted with respect to the systemic velocity, we repeat this exercise in the 8500-8700 Å region where we see a subtle, broad 'bump' in the QSO spectrum, but find no evidence for extended emission in this region either. Unfortunately these results do not place any strong constraint on the powering mechanism of this Lyα halo; i.e. in the absence of strong radio emission CIV luminosities are so much fainter than Lyα emission (e.g. typically CIV/Ly$\alpha \leq 0.13$ in Lyα 'blobs' where no definitive power source has been determined; Arrigoni Battaia et al. 2018). Although radio continuum has been observed in both the QSO and SMG here, the emission is consistent with a weak AGN or extreme star formation (Yun & Carilli 2002, Carilli et al. 2013) and not the powerful high-redshift radio galaxies (HzRGs) that are known to exhibit significant extended CIV (e.g. Matsuoka et al. 2009).

4. COMPANIONS IN THE FIELD

In this Section, we present new spectra from MUSE of the two known LAEs in addition to LAE 3 discovered in this work. We present measurements of the Lyα flux, velocity width, and rest-frame equivalent width (EW_0), and discuss the results below. In addition we investigate the existence of an additional source, dubbed "SRC 6", motivated by an alignment of dust continuum emission and a compact object seen in HST775W imaging. The diversity of object properties (and their staggered discovery) means that the dataset in which each object's position is defined varies. Where possible, we take the object's position directly from table 1 of Carilli et al. 2013 (i.e. for the QSO, SMG, LAE 1, and LAE 2). For the QSO, SMG and LAE 2 this is the dust continuum position. For LAE 1 this is the [CII] position. LAE 3 is defined by its MUSE detection, and the position of SRC 6 is defined as the centre of the dust emission.

4.1. *Lyα properties of companions*

In Table 2 we summarise our measurements of Lyα emission from the MUSE cube for each of the objects known in the BR1202 − 0725 field, plus LAE 3, and the potential source 'SRC 6'. We also include cutout images and spectra in Appendix A to demonstrate our choice of aperture size, and the MUSE spectrum from which we measure the Lyα flux (Table 2 column 5).

The complexity of the BR1202 − 0725 system and the diffuse Lyα emission in the field make it difficult to identify individual objects' Lyα in an image, as objects are essentially 'embedded' within the diffuse Lyα halo stretching across the entire field. For this reason we choose very narrow velocity ranges over which we display the corresponding Lyα image in the final column of Figure 7. We then choose an aperture on these images to encapsulate the emission from a particular object.

For two objects, LAE 1 and LAE 3, the Lyα flux can be estimated simply by fitting a Gaussian profile to the 1D spectral extraction. For these two objects we also place constraints on the rest-frame equivalent width (EW_0) of Lyα from the MUSE spectrum. Accurate measurements of LAEs' EW_0 at this redshift are potentially of great interest due to their ability to distinguish between powering mechanisms of Lyα emission. Models based on standard IMFs, stellar populations and metallicity ranges for instance predict a maximum value of $EW_0 = 240$Å for emission powered by star formation (see Schaerer 2003 and Hashimoto et al. 2017). For LAE 2 it is difficult to produce a good fit from the 1D spectrum, and so we first fix the peak of the Gaussian to the predicted wavelength of Lyα emission corresponding to LAE 2's systemic redshift. For the remaining objects (the QSO, the SMG, and 'SRC 6') we simply sum the flux across a 50 Å window (i.e. $\approx$ twice the measured FWHM of LAE 1).

We recover a Lyα flux estimate for LAE 1 of $F_{Ly\alpha} = 1.54 \pm 0.05 \times 10^{-16}$ erg s^{-1} cm^{-2} over an aperture of diameter 1.5″. This flux measurement and its associated velocity width and EW_0 can be compared to literature values from long-slit spectroscopy presented in Williams et al. (2014). Our flux measurement for LAE 1 is actually somewhat smaller than the literature result ($F_{Ly\alpha} = 2.53 \pm 0.08 \times 10^{-16}$ erg s^{-1} cm^{-2}), possibly due to the halo contaminating the end of the long slit[5] but we find a large velocity width of FWHM $=1149 \pm 45$ km s^{-1}, almost consistent with the literature value (FWHM $=1381 \pm 124$ km s^{-1}). We also measure the equivalent width, and find EW_0(Lyα)$= 72.9 \pm 2.2$ Å. This is a fairly large EW_0, although smaller than the published estimate ($EW_0 = 103 \pm 15$ Å) from long-slit spectroscopy. The difference is possibly explained by factors such as contamination of the long slit by light from the QSO (which would boost the measured Lyα flux and hence the EW_0). Even so, our flux estimate may be subject to overestimating the Lyα originating within LAE 1 as we too observe the object through the QSO's Lyα halo, and fit a 1D Gaussian fit to this line. Conversely however, factors such as underestimating the true extent on-sky of LAE 1 and the inaccuracy of a Gaussian fit may result in our missing some flux.

LAE 2 has a low Lyα flux with emission that appears diffuse on-sky, and with a large velocity width. Taking an aperture of 1.5″ in diameter driven by the object's appearance in HST imaging, we measure a flux of $F_{Ly\alpha} = 0.54 \pm 0.05 \times 10^{-16}$ erg s^{-1} cm^{-2}, and a velocity width of FWHM $= 2480 \pm 275$ km s^{-1}. The numbers we derive are similar to previous results (Williams et al. 2014 measure a flux of $F_{Ly\alpha} = 0.33 \pm 0.06 \times 10^{-16}$ erg s^{-1} cm^{-2}, a velocity width of FWHM $=1225 \pm 257$ km s^{-1}, and an EW of $EW_0 = 67 \pm 15$ Å).

In the vicinity of the SMG we measure faint Lyα emission, but are unable to force a fit to this line in order to measure a flux, velocity width, or EW_0. Summing the flux over 50 Å (for consistency with LAE 1), in an aperture of diameter 1.5″, we measure a low-level of Lyα emission at $F_{Ly\alpha} = 0.04 \pm 0.01 \times 10^{-16}$ erg s^{-1} cm^{-2}.

Next we measure a Lyα flux and line properties for the newly discovered source LAE 3. We find a flux of $F_{Ly\alpha} = 0.24 \pm 0.03 \times 10^{-16}$ erg s^{-1} cm^{-2} over a diameter of 1.5″. The velocity width measures FWHM $= 471 \pm 62$ km s^{-1}, significantly narrower than LAE 1, or indeed any of the other objects in the system. We do not see continuum emission from LAE 3 in the MUSE data, therefore we place a lower limit on EW_0 of LAE 3. To do so, we use the RMS of an image of $\Delta\lambda = 700$ Å, redward of the emission line, to place an upper limit on the continuum, and in combination with the flux measurement, derive a $5\,\sigma$ upper limit of $EW_0(Ly\alpha^{lim}_{5\sigma}) \geq 34.05$ Å.

The final object for which we measure a Lyα flux is "SRC 6". Motivated by an alignment of dust continuum emission and a compact object seen in HST775W, we extracted a spectrum at the HST775W position to search for Lyα emission. We see no evidence for significant Lyα emission originating from the object seen in HST imaging, although a marginal detection is seen ~ 0.2″ South. We report in Table 2 the flux seen in a 1 ″ aperture at this position, and the redshift if the corresponding tentative detection in the ALMA cube is [CII] emission.

4.2. *Nature of companions*

In combination with our measurements of Lyα emission from the sources in this field, we use existing ALMA data to compare the Lyα and [CII] images and spectra, together with high-resolution optical HST775W images, and our dust-continuum map from ALMA. We evaluate the most likely physical scenarios leading to each object's appearance in these datasets based on Figure 6, also taking note of the channel maps shown in Appendix B. In each row of Figure 6 we show a single object. In the left-hand panel, we show an HST775W image representative of the optical stellar light, overlaid with Lyα

[5] See figure 1 in Williams et al. 2014 for their slit placement.

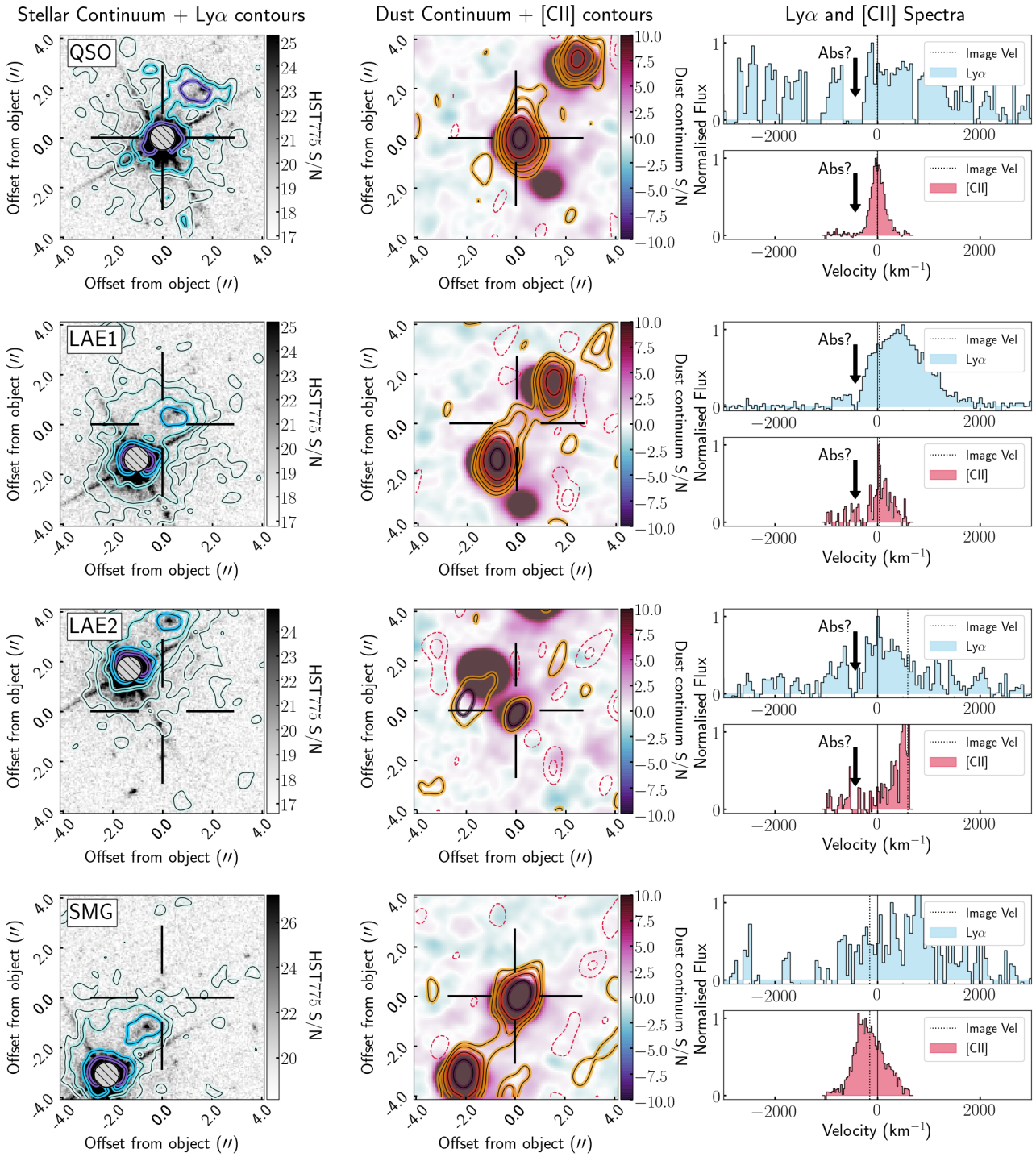

Figure 6. Cutout images and spectra of companion objects in the vicinity of the QSO-SMG system at $z \sim 4.7$. In the left-hand panels we show a cutout of the object in the HST775W image, overlaid with Lyα contours (log-spaced with the lowest contour at 1σ) from the MUSE cube, at the velocity of interest (either λ Ly$\alpha_{[\mathrm{pred}]}$, or the peak of the Lyα emission if there is no [CII] detection). In the central panels we take the same approach using the sub-mm data, and show a cutout of the object from the ALMA dust continuum map, overlaid with contoured [CII] emission at the relevant velocity (contours are log-spaced with the lowest contour at 1.5 σ). In the right-hand panels we show Lyα and [CII] spectra extracted within the aperture shown on the left-hand side. On the spectra a dotted black line represents the velocity shown in contours. For the relevant objects (The QSO, LAE 1 and LAE 2) we incude an arrow to indicate the coherent absorption feature seen in these objects. Figure continues on next page.

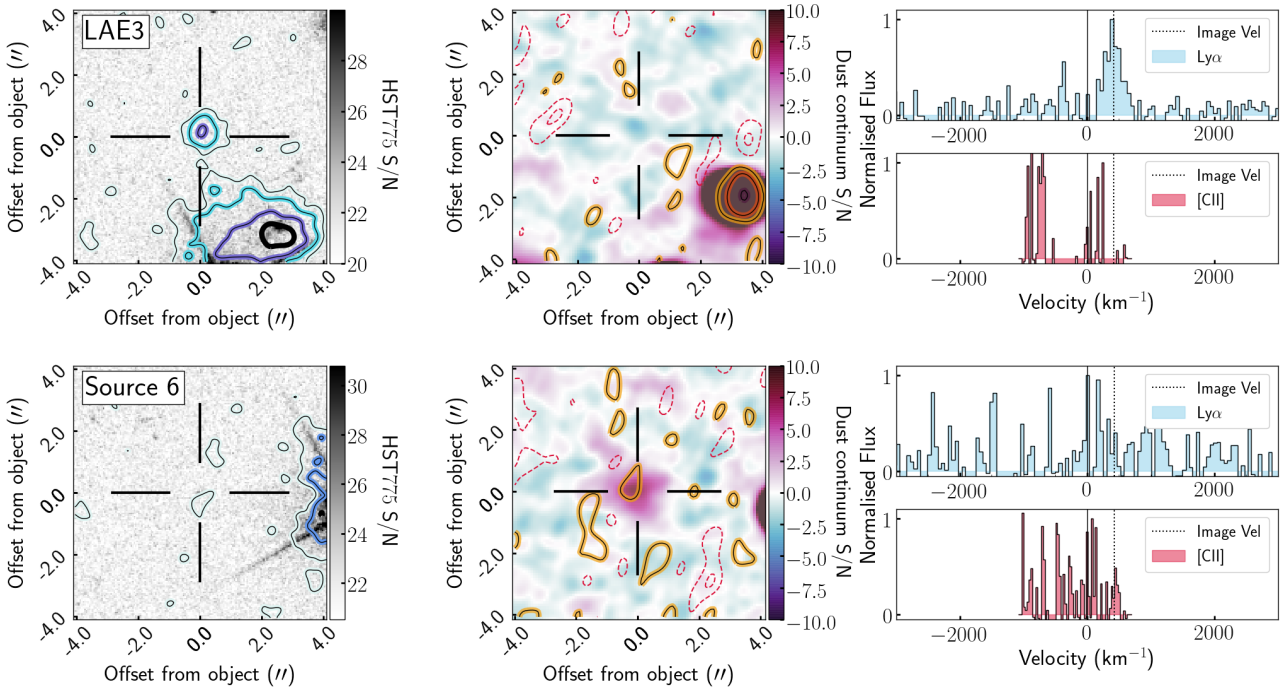

Figure 6. Continued as on previous page.

Table 2. Lyα measurements for each object in the system. The first column gives the name for each object. The second column gives a position (see text for details). The third column gives the best estimate of the object's redshift; either the [CII] redshift from Carilli et al. (2013), or the Lyα redshift measured here. The fourth column gives the observed peak wavelength of Lyα emission from fitting the peak of the 1D spectra. The fifth column gives the flux within an aperture of 1.5″ in diameter (except for the QSO halo, and SRC 6 - see footnotes). The sixth column gives the velocity width of the Lyα line (FWHM), where it was possible to fit the 1D spectrum with a Gaussian. The seventh column gives the rest-frame Lyα equivalent width (or a 5σ lower limit) where appropriate. The last column gives the SFR calculated from each object's Lyα emission, again where appropriate.

Object	**Position** [J2000]	$z_{\rm best}$	$\lambda_{\rm Obs\,Ly\alpha}$ [Å]	$\mathbf{F}_{\rm Ly\alpha}$ (10^{-16}) [erg s^{-1} cm^{-2}]	**fwhm**$_{\rm Ly\alpha}$ [km s^{-1}]	**EW**$_{0\,\rm Ly\alpha}$[a] [Å]	**SFR**$_{\rm Ly\alpha}$ [$M_\odot$ yr^{-1}]
QSO	J120523.13-074232.6	4.6942[b]	No peak	13.9 ± 0.18[c]	–	–	296.0 ± 4.0
SMG	J120522.98-074229.5	4.6915[b]	6941.86	0.12±0.02	–	–	–
LAE 1	J120523.06-074231.2	4.6950[b]	6932.25	1.54±0.05	1149±45	72.9 ± 2.2	32.9±3.3
LAE 2	J120523.04-074234.3	4.7055[b]	6936.00 (fix)	0.54±0.05	2480±275	–	–
LAE 3	J120523.19-074227.7	4.7019[d]	6931.65	0.24±0.03	471±62	$\geq 34.05\,^{lim}_{5\sigma}$	5.0±0.5
SRC 6	J120523.46-074232.1	4.7035[b]	6932.44 (fix)	0.03±0.01	–	–	–

[a] $\rm EW_0 = (F_{Ly\alpha}/F_{cont}) \times (1/(1 + z_{best}))$.

[b] $z_{\rm [CII]}$

[c] For the QSO halo we report the flux summed within the SB $> 10^{-17}$ erg s^{-1} cm^{-2} arcsec^{-2} contour across the entire field. Both the residuals from PSF subtraction, and the position of LAE 1 are masked.

[d] $z_{\rm Lya}$

contours extracted from the MUSE cube at the redshift of the object. These cutouts demonstrate the extended nature of Lyα emission compared to our previous best impression of the objects' optical sizes. In the central panel we show a dust-continuum map, overlaid with contours depicting [CII] emission at each object's peak velocity. Finally in the right-hand panels we show the Lyα and [CII] spectra in velocity space, relative to the systemic redshift of the QSO.

Interestingly, for those objects with [CII] emission (and hence a systemic redshift), it is not evident that Lyα emission is always present at the same velocity, or even at the objects' positions on-sky at all. Likewise, the brightest objects shining in Lyα do not always correspond to a detection in [CII].

4.2.1. *QSO*

The QSO's continuum and PSF-subtracted spectrum were shown in Figure 3, and we discussed the flux measurement in Section 3.1. No distinct 'peak' is seen at the predicted wavelength of Lyα, but copious amounts of emission remain across a broad range of velocities. As seen in Figure 3, when the emission greater than 1×10^{-17} erg s^{-1} cm^{-2} arcsec^{-2} is summed, the line profile becomes more centrally concentrated in wavelength. The most striking feature of this spectrum is the distinct absorption feature seen at ≈ 6912 Å. The absorption saturates indicating a high column density of HI gas approximately 400 km s^{-1} from the QSO. This kind of signature has sometimes been interpreted in the literature as an expanding shell of neutral gas surrounding a QSO (e.g. van Ojik et al. 1997, Binette et al. 2000).

4.2.2. *SMG*

In the literature, optical emission from the SMG has evaded detection. As described above, in the MUSE datacube we place an aperture at the position of the SMG and are able to measure Lyα emission which would be equivalent to an instantaneous SFR$_{\mathrm{Ly}\alpha} \approx 2$ M$_\odot$ yr^{-1}. The line profile however is remarkably similar to the QSO's Lyα halo, and indeed no source is visible by eye in the Lyα channel maps at the position of SMG. We conclude that the Lyα line detected at this position arises from the edge of the QSO's extended Lyα halo, and so we choose not to report a Lyα velocity width, EW$_0$ or SFR for the SMG in Table 2. The channel maps in Appendix B present interesting features in the Lyα emission in the vicinity of the SMG. In particular, multiple channels spanning a few hundred km s^{-1} display very low surface brightness emission elongated west of the SMG.

4.2.3. *LAE 1*

LAE 1 is well-studied, and the measurements we report here are broadly consistent with literature results. As already noted by other studies, including Williams et al. (2014), the EW$_0$(Lyα) is high, although it is consistent with being powered by star formation. In addition Williams et al. (2014) argue that since no CIV or HeII emission is detected in this source, there can be at most a 10% contribution to LAE 1's Lyα flux from AGN-powered photoionisation. So in conclusion there may be multiple powering mechanisms at work for the Lyα emission falling into the aperture. (A) Some star formation occurring within LAE 1, (B) perhaps up to a 10% contribution from an AGN, and (C) the Lyα halo extending from the QSO, within which LAE 1 is embedded. Previous measurements of the SFR using various techniques reported values for LAE 1 in the range SFR$_{\mathrm{UV}}$= 13M$_\odot$ yr^{-1} (Ohyama et al. 2004), to SFR$_{\mathrm{[CII]}}$= 19M$_\odot$ yr^{-1} (Williams et al. 2014). Transforming our Lyα flux to a star formation rate we find an SFR$_{\mathrm{Ly}\alpha} \approx 32 \pm 3$ M$_\odot$ yr^{-1}. We also note that the Lyα line profile is symmetric, which is not always typical of LAEs at high redshift due to the very low neutral fraction (10^{-4}) required to absorb all photons blue-ward of 1215.67 Å, often leading to an asymmetric line (e.g. Fan et al. 2001). Williams et al. (2014) were the first to infer that the symmetric profile of LAE 1 places a constraint on the size of the ionised bubble surrounding QSO BR1202 − 0725, and we concur with this conclusion. Finally we note that the absorption feature visible clearly in the spectrum of the QSO at $\approx$ 6912 Å is also seen in the spectrum of LAE 1, requiring that photons from the LAE as well as the QSO (some 15 pkpc apart) encounter the same barrier of neutral gas.

The peak of the Lyα emission from LAE 1 falls at 6932 Å, offset in velocity by $\sim$397 km s^{-1} from the predicted position according to the peak of [CII] in LAE 1. Note this is greater than the previously reported value in the literature due to our velocity frame correction (Section 2.2.2). Upon close inspection of the channel maps shown in Appendix B, it is interesting to note that the [CII] coordinate reported for LAE 1 (most apparent in the channel at 23.93 km s^{-1} is offset by $\approx 0.6''$, although the aperture within which we extract spectra and measure flux contains both peaks. Furthermore, the purported [CII] "bridge" of emission between the QSO and the SMG, appears to 'swirl' around the position of LAE 1– appearing for instance both to the East and to the West of the Lyα peak of LAE 1 at velocities either side of the peak. Assuming that both the [CII] and Lyα emission originate from the source known as LAE 1, this could be indicative for example of tidal disruption of LAE 1's ISM during a merger between itself, the SMG,

and the QSO. Regardless, we conclude that LAE 1 is indeed likely to be a star-forming LAE associated with this group of merging galaxies, and embedded within the extended Lyα halo of the QSO, possibly shielded by an expanding 'shell' of optically thick gas giving rise to the absorption feature.

4.2.4. *LAE 2*

As we reported in section 4.1, the Lyα line that we measure is broad, and offset in velocity from the [CII] line at the position of LAE 2. Until now this has not presented difficulty for the physical interpretation of Lyα emission in the vicinity of LAE 2. Taking advantage of the simultaneous spectral and spatial coverage of MUSE however, we see that the Lyα emission line profile is remarkably similar to that from the QSO's halo. Furthermore, although LAE 2 appears distinct in HST775W imaging, stepping through channels of the MUSE cube, no particular layer shows spatially-peaked Lyα emission relative to the diffuse emission across the field. Specifically, we check the predicted wavelength of Lyα from LAE 2's [CII] emission, but in addition extend the search outward to both positive and negative velocities. No spectral region suggests the presence of an object in the MUSE datacube. This implies that perhaps the emission seen in HST775W is stellar continuum, which is outshone by diffuse Lyα in the BR1202 − 0725 halo in the MUSE cube. Indeed, we see in the channel maps that diffuse Lyα emission appears to extend towards the position of LAE 2 in the velocity channels preceding LAE 2 – we speculate that LAE 2 is perhaps passing through the QSO's Lyα halo, with a peculiar velocity directly away from the observer. From the information added here from MUSE, we conclude that the object often referred to in the literature as 'LAE 2' is in fact not responsible for powering the Lyα emission seen at this position in previous datasets, and this Lyα line is entirely consistent with being part of the extended halo surrounding QSO BR1202 − 0725. We do once again see the absorption feature at 6912Å, indicating that this position on sky is also covered by the absorbing gas.

4.2.5. *LAE 3*

The newly discovered LAE 3 shows a bright Lyα line peaking at 6931Å, placing the LAE at a redshift of $z_{Ly\alpha} = 4.7019$. We measure properties for LAE 3 more consistent with typical LAEs at high redshift e.g. Drake et al. (2017a), Drake et al. (2017b), Hashimoto et al. (2017), Wisotzki et al. 2016, Leclercq et al. 2017. The measured flux for LAE 3 translates to an SFR = 5±0.5 $M_\odot\,yr^{-1}$. We place a lower limit on the EW_0 of LAE 3 of $EW_0(Ly\alpha\,^{lim}_{5\sigma}) \geq 34.05$ Å. This is consistent with in-situ star formation as the primary power source of the Lyα line, although we cannot rule out contributions from an AGN, or perhaps the edge of the QSO's halo also.

No [CII] or dust continuum emission is detected at the position of LAE 3. This is not altogether surprising, given the young ages and low metallicities typical of the high-redshift LAE population. Therefore LAE 3 is most likely to be a star-forming LAE at the redshift of the QSO. Interestingly, the profile of the Lyα line appears symmetric just as in LAE 1. Following the arguments in Williams et al. (2014), we here propose that the symmetric profile of LAE 3 indicates a new lower limit on the radius of the HII sphere/proximity zone of QSO BR1202 − 0725, at some ∼ 30 pkpc away (also see Bosman et al. 2019 for a discussion on proximate LAEs at high redshift). Finally, the coherent absorption feature seen in the spectra of the other objects is at a bluer wavelength than the edge of this narrow Lyα line, and as such we cannot say if the proposed absorbing shell extends to the position of LAE 3.

4.2.6. *SRC 6*

The teamSRC 6 is detected primarily in the dust continuum. In addition, we see tentative [CII] emission coincident with part of the area of dust emission, and an even less convincing Lyα detection. If the [CII] detection is real, this places the object at $z = 4.7025$. It is notable also, that low-surface-brightness Lyα emission in this region could once again be part of the QSO's Lyα halo, appearing coincident with an unrelated object along the line of sight.

5. SUMMARY

We have presented new optical IFU data from MUSE across the BR1202 − 0725 field, which is one of the most overdense regions of the early Universe known at $z = 4.69$. BR1202 − 0725 is clearly a very extreme system, undergoing a major merger and demonstrating drastic tidal disruption of the smaller galaxies in the vicinity. Prior to this work BR1202 − 0725 was already one of the most studied single-targets at high redshift, acting as a laboratory for the study of diverse galaxies typically detected via different selection techniques, all evolving in the same environment. Here, we examine the Lyα halo surrounding QSO BR1202 − 0725 and measure Lyα properties for companions in the field, including a new LAE discovered in this work. In conjunction with existing ALMA observations we examine and compare the neutral and ionised gas content of the BR1202 − 0725 system's Lyα halo and constituent objects, which provides us with the best view to date of the physical processes under way in BR1202 − 0725 until new facilities (e.g. JWST and the GTO programme)

become available. Our main findings can be summarised as follows:

- QSO BR1202 − 0725 exhibits a large Lyα halo, stretching across at least $\sim 8''$ on-sky (≈ 55 pkpc at $z = 4.6942$) at surface brightness levels greater than 1×10^{-17} erg s^{-1} cm^{-2} arcsec^{-2}.

- In contrast, no Lyα halo is detected around the SMG, which has a similar gas mass and SFR as the QSO.

- We do not find evidence for extended CIV emission surrounding the QSO down to a surface brightness limit of SB $\approx 0.19 \times 10^{-16}$ erg s^{-1} cm^{-2} arcsec^{-2} in a square arcsecond, and hence can not place any constraint on the dominant powering mechanism of the Lyα halo.

- The optical NW-companion of QSO BR1202 − 0725 known as "LAE 1" appears to be a Lyα-emitting galaxy embedded within the larger region of diffuse Lyα emission. Taking an aperture of $2''$ in diameter we measure a Lyα flux, velocity width consistent with literature measurements from long-slit spectra. We measure an EW$_0$(Lyα)$= 72.9 \pm 2.2$ Å, this is probably due to a combination of powering mechanisms for the Lyα.

- The optical SW-companion of QSO BR1202 − 0725, confirmed in [CII] and [NII] emission, known as "LAE 2" is not necessarily responsible for the Lyα emission previously reported at this position. Although we detect a Lyα line, it appears diffuse on-sky, with no local maximum coinciding with the position of LAE 2. The Lyα line profile, peak, and FWHM are also more consistent with being part of the QSO's diffuse halo.

- We detect an additional LAE in the BR1202 − 0725 system $\sim 5''$ to the north of the QSO, and denote it "LAE 3". The object was discovered serendipitously in the MUSE datacube, and exhibits a bright but narrow Lyα line of flux $0.24 \pm 0.03 \times 10^{-16}$ erg s^{-1} cm^{-2} ($1.5''$), a velocity width of 471.23 km s^{-1} and EW$_0$(Ly$\alpha\,^{lim}_{5\sigma}$) $\geq$ 34.05 Å. This LAE is more aligned with typical properties of Lyα emitters at high redshift, with Lyα emission consistent with powering by star formation.

- The symmetric profile of Lyα in LAE 3 places a new constraint on the size of the HII bubble surrounding QSO BR1202 − 0725 of $\approx$ 60 pkpc in diameter.
- We see coherent absorption, possibly indicative of an expanding shell of HI gas, 400 km s^{-1} infront of BR1202 − 0725 across at least $4''$ on-sky, corresponding to ∼24 pkpc (diameter). The feature is blue-ward of the edge of Lyα from LAE 3 and hence we cannot confirm whether LAE 3 is covered by the HI gas.

These results demonstrate the efficiency of MUSE for detecting low-surface-brightness Lyα emission in addition to the instrument's use as a 'redshift machine' for the detection of emission-line galaxies. Futhermore, the combined power of MUSE and ALMA to examine both ionised- and cool gas components offers unprecedented insights on the nature of a diverse population of objects at high redshift. This work also highlights the need for follow-up of Lyα halos with future facilities (such as JWST) with a view to unambiguously detecting/ruling out the presence of e.g. metal lines, to finally disentangle the processes powering these giant structures.

ABD, FW, MN and MN acknowledge support from the ERC Advanced Grant 740246 (Cosmic Gas).

This paper makes use of the following ALMA data: ADS/JAO.ALMA#2011.0.00006.SV, 2013.1.00039.S, 2013.1.00259.S, 2013.1.00745.S, 2015.1.00388.S, 2015.1.01489.S, 2017.1.00963.S, 2017.1.01516.S. ALMA is a partnership of ESO (representing its member states), NSF (USA) and NINS (Japan), together with NRC (Canada), NSC and ASIAA (Taiwan), and KASI (Republic of Korea), in cooperation with the Republic of Chile. The Joint ALMA Observatory is operated by ESO, AUI/NRAO and NAOJ.

Software: Astropy (Astropy Collaboration et al. 2013); CASA (McMullin et al. 2007), MUSE data reduction pipeline (Weilbacher et al. 2012), (Weilbacher et al. 2014), ZAP (Soto et al. 2016), MPDAF (Piqueras et al. 2017).

APPENDIX

A. APPENDIX A

We include here in Figure 7 the spectra and images from which we measure the Lyα properties of each source. In the left-hand panels we show a cutout of the object in the high-resolution HST775W image, in the central panels we show

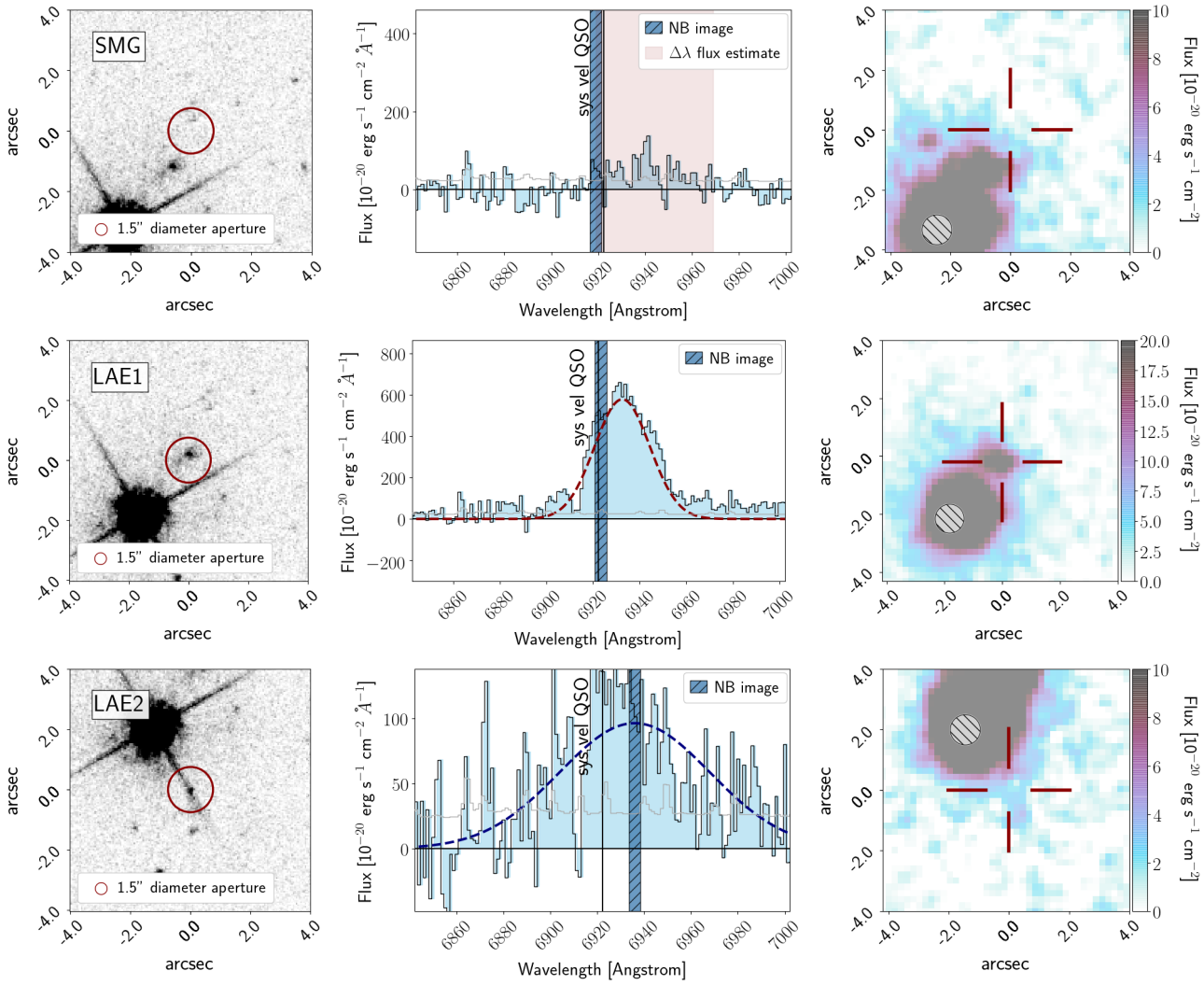

Figure 7. Cutout images and spectra of companion objects in the vicinity of the QSO-SMG system at $z \sim 4.7$. Figure continues on next page.

a spectrum extracted from the MUSE cube within the aperture shown on the HST775W image, and in the right-hand panels we show a cutout image extracted from the MUSE cube across the wavelength range shaded in orange on the spectrum. Apertures are centred on the [CII] positions reported in Carilli et al. (2013) where possible, otherwise the peak of the Lyα emission seen in MUSE is taken. For the objects where no 1D Gaussian fit could be performed, we shade in red the region of the spectrum which is summed to estimate the Lyα flux.

B. APPENDIX B

This appendix contains the MUSE and ALMA channel maps depicting the extended Lyα and [CII] emission at a series of velocities relative to the QSO's systemic redshift in Figure 7.

C. APPENDIX C

This appendix demonstrates our search for extended CIV emission surrounding QSO BR1202 − 0725 discussed in Section 3.4.

REFERENCES

Arrigoni Battaia, F., Hennawi, J. F., Prochaska, J. X., & Cantalupo, S. 2015a, ApJ, 809, 163

Arrigoni Battaia, F., Hennawi, J. F., Prochaska, J. X., et al. 2019, MNRAS, 482, 3162

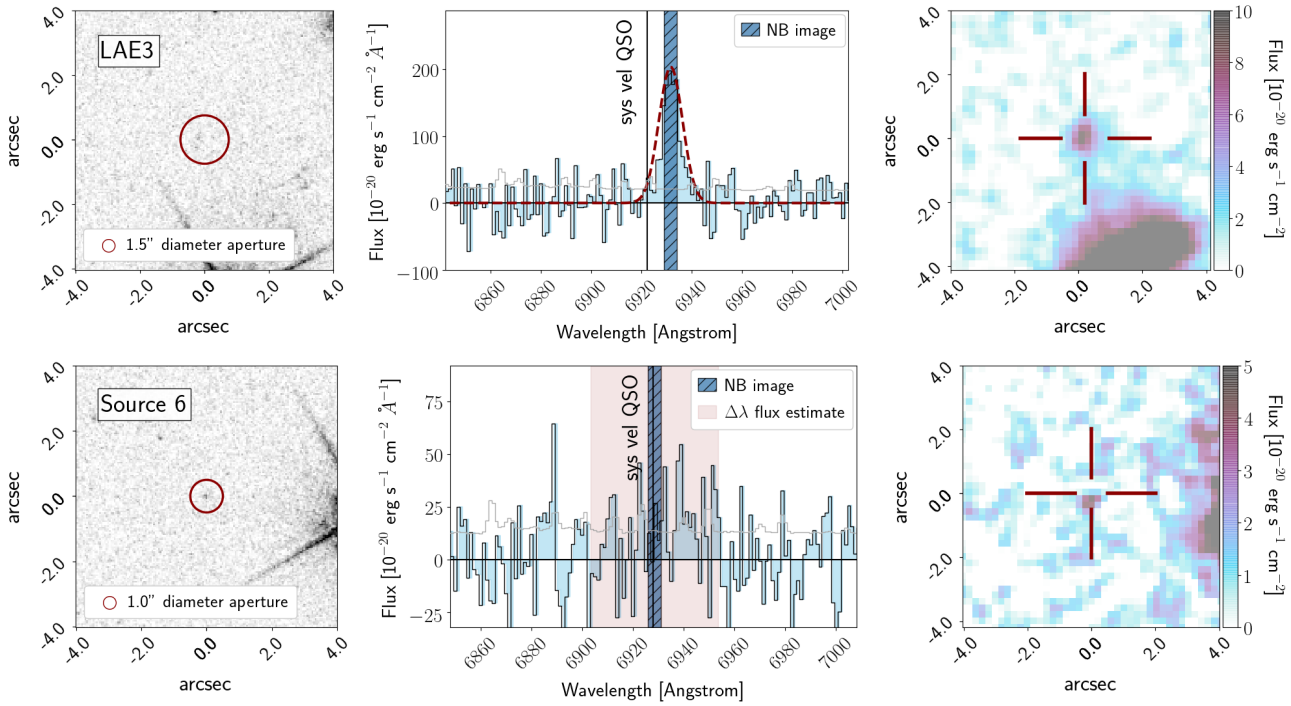

Figure 7. Continued as on previous page.

Arrigoni Battaia, F., Yang, Y., Hennawi, J. F., et al. 2015b, ApJ, 804, 26

Arrigoni Battaia, F., Chen, C.-C., Fumagalli, M., et al. 2018, A&A, 620, A202

Astropy Collaboration, Robitaille, T. P., Tollerud, E. J., et al. 2013, A&A, 558, A33

Bacon, R., Accardo, M., Adjali, L., et al. 2010, in Proceedings of the SPIE, Volume 7735, id. 773508 (2010)., ed. I. S. McLean, S. K. Ramsay, & H. Takami, Vol. 7735, 773508

Bacon, R., Brinchmann, J., Richard, J., et al. 2015, A&A, 575, A75

Bacon, R., Conseil, S., Mary, D., et al. 2017, A&A, 608, A1

Binette, L., Kurk, J. D., Villar-Martín, M., & Röttgering, H. J. A. 2000, A&A, 356, 23

Borisova, E., Cantalupo, S., Lilly, S. J., et al. 2016, arXiv:1605.01422

Bosman, S. E. I., Kakiichi, K., Meyer, R. A., et al. 2019, arXiv e-prints, arXiv:1912.11486

Cai, Z., Cantalupo, S., Prochaska, J. X., et al. 2019, ApJS, 245, 23

Cantalupo, S. 2010, MNRAS, 403, L16

Carilli, C. L., Riechers, D., Walter, F., et al. 2013, ApJ, 763, 120

Carniani, S., Marconi, A., Biggs, A., et al. 2013, A&A, 559, A29

Daddi, E., Valentino, F., Rich, R. M., et al. 2020, arXiv e-prints, arXiv:2006.11089

Decarli, R., Walter, F., Venemans, B. P., et al. 2017, Nature Publishing Group, 545, doi:10.1038/nature22358

Drake, A. B., Farina, E. P., Neeleman, M., et al. 2019, ApJ, 881, 131

Drake, A. B., Guiderdoni, B., Blaizot, J., et al. 2017a, Monthly Notices of the Royal Astronomical Society, 471, 267

Drake, A. B., Garel, T., Wisotzki, L., et al. 2017b, Astronomy & Astrophysics, 608, A6

Fan, X., Narayanan, V. K., Lupton, R. H., et al. 2001, The Astronomical Journal, 122, 2833

Farina, E. P., Venemans, B. P., Decarli, R., et al. 2017, The Astrophysical Journal, 848, 78

Farina, E. P., Arrigoni-Battaia, F., Costa, T., et al. 2019, ApJ, 887, 196

Ginolfi, M., Maiolino, R., Carniani, S., et al. 2018, Monthly Notices of the Royal Astronomical Society, 476, 2421

Hashimoto, T., Garel, T., Guiderdoni, B., et al. 2017, A&A, 608, A10

Hu, E. M., McMahon, R. G., & Egami, E. 1996, ApJL, 459, L53

Hu, E. M., McMahon, R. G., & Egami, E. 1997, in The Hubble Space Telescope and the High Redshift Universe, ed. N. R. Tanvir, A. Aragon-Salamanca, & J. V. Wall, 91

Inami, H., Bacon, R., Brinchmann, J., et al. 2017, A&A, 608, A2

Iono, D., Yun, M. S., Elvis, M., et al. 2006, ApJL, 645, L97

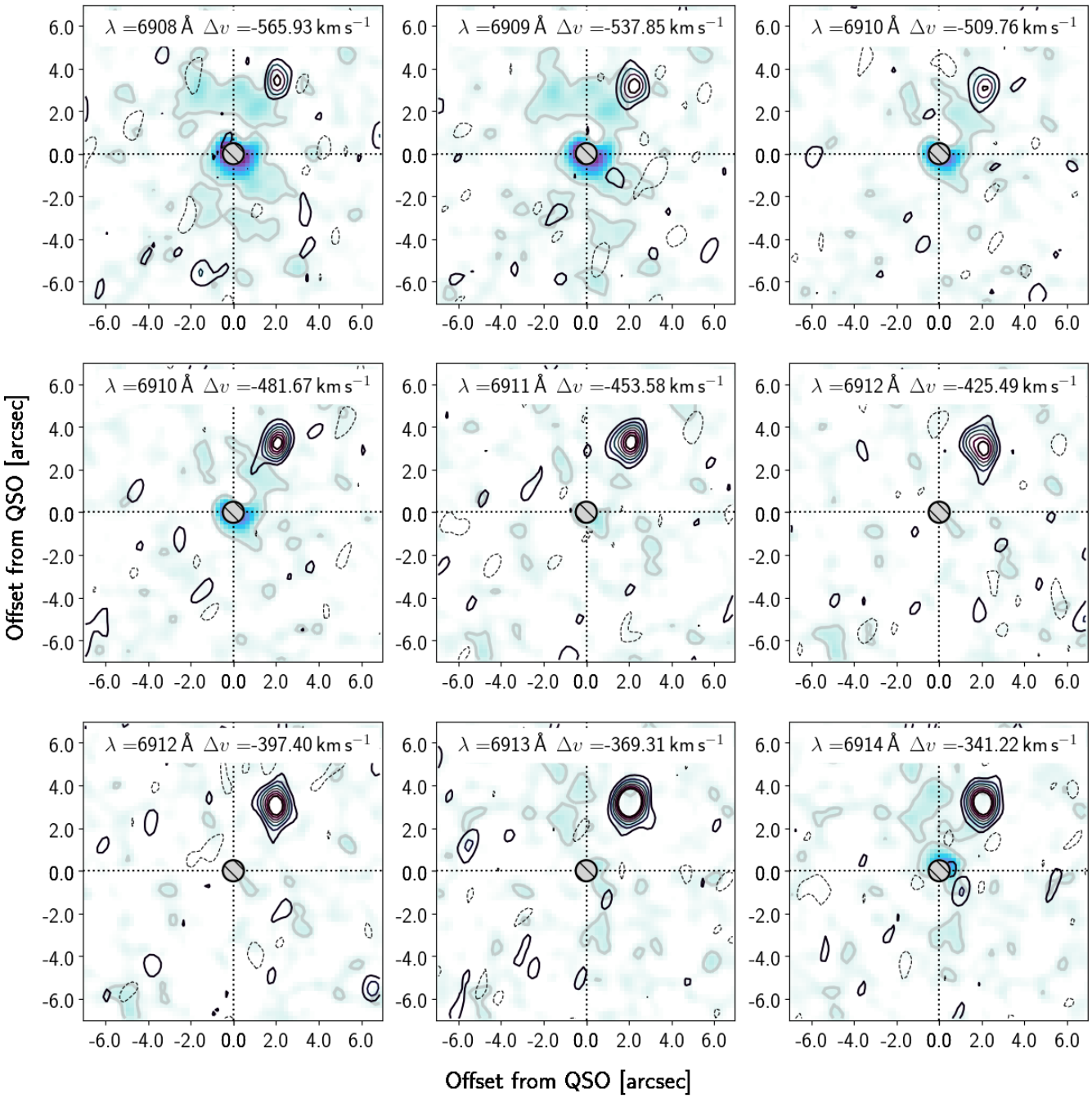

Figure 8. MUSE Lyα channel-maps, overlaid with [CII] contours from ALMA, where contours are linearly spaced at $\pm$ 1.5, 3.0, 6.0, 9.0, 12.0 and 15.0 σ, and negative contours are represented by dotted lines. MUSE data have been rebinned in velocity for comparison to the lower velocity resolution of the ALMA channels. Figure continues on next page.

Irwin, M., McMahon, R. G., & Hazard, C. 1991, in Astronomical Society of the Pacific Conference Series, Vol. 21, The Space Distribution of Quasars, ed. D. Crampton, 117–126

Isaak, K. G., McMahon, R. G., Hills, R. E., & Withington, S. 1994, MNRAS, 269, L28

Leclercq, F., Bacon, R., Wisotzki, L., et al. 2017, Astronomy & Astrophysics, 608, A8

Lee, M. M., Nagao, T., De Breuck, C., et al. 2019, ApJL, 883, L29

Lehnert, M. D., Yang, C., Emonts, B. H. C., et al. 2020, arXiv e-prints, arXiv:2004.04176

Marino, R. A., Cantalupo, S., Pezzulli, G., et al. 2019, ApJ, 880, 47

Matsuoka, K., Nagao, T., Maiolino, R., Marconi, A., & Taniguchi, Y. 2009, A&A, 503, 721

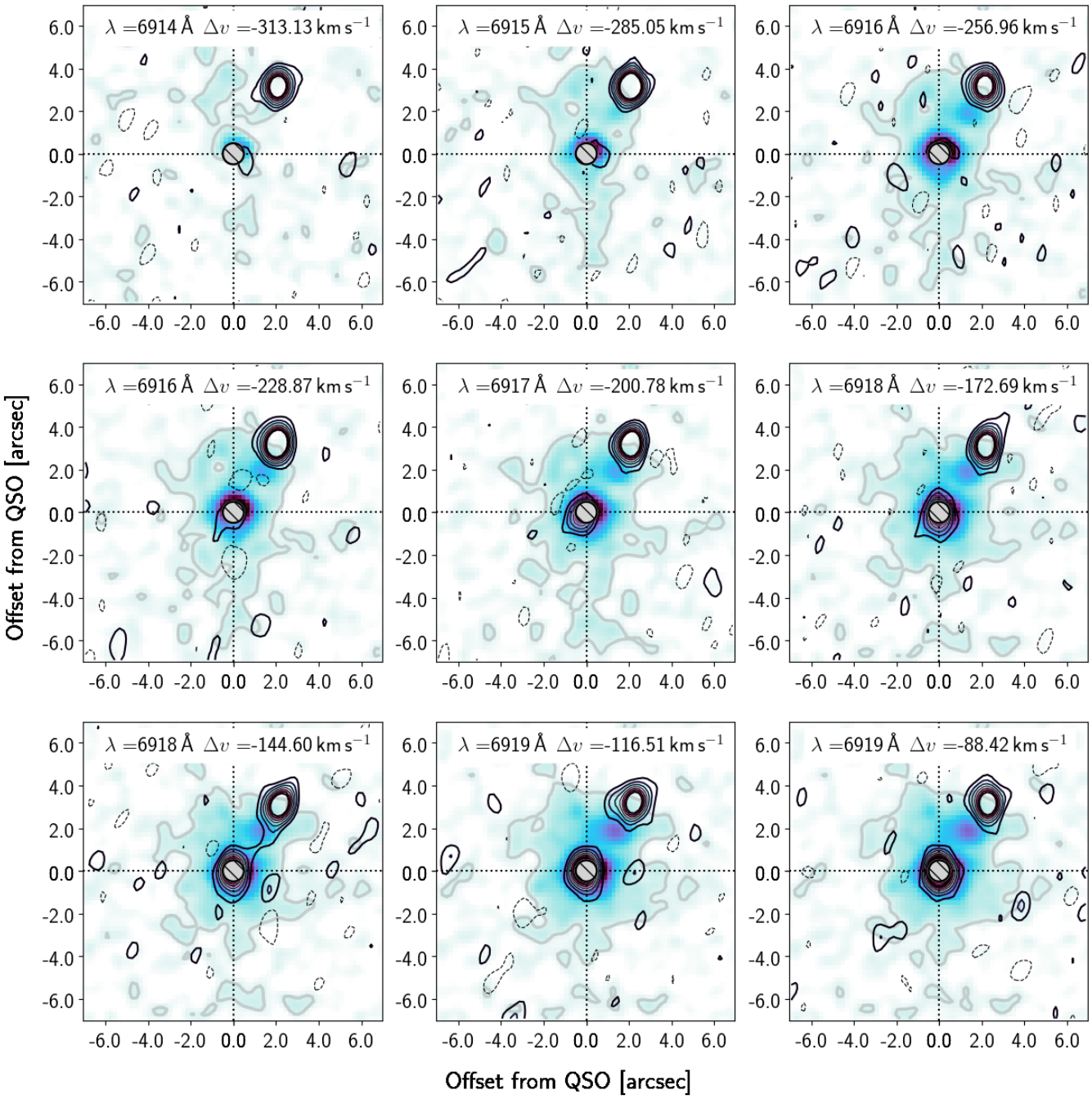

Figure 8. Continued from previous page.

McMahon, R. G., Omont, A., Bergeron, J., Kreysa, E., & Haslam, C. G. T. 1994, MNRAS, 267, L9

McMullin, J. P., Waters, B., Schiebel, D., Young, W., & Golap, K. 2007, Astronomical Society of the Pacific Conference Series, Vol. 376, CASA Architecture and Applications, ed. R. A. Shaw, F. Hill, & D. J. Bell, 127

Michel-Dansac, L., Blaizot, J., Garel, T., et al. 2020, A&A, 635, A154

Ohta, K., Yamada, T., Nakanishi, K., et al. 1996, Nature, 382, 426

Ohyama, Y., Taniguchi, Y., & Shioya, Y. 2004, AJ, 128, 2704

Omont, A., McMahon, R. G., Cox, P., et al. 1996a, A&A, 315, 1

Omont, A., Petitjean, P., Guilloteau, S., et al. 1996b, Nature, 382, 428

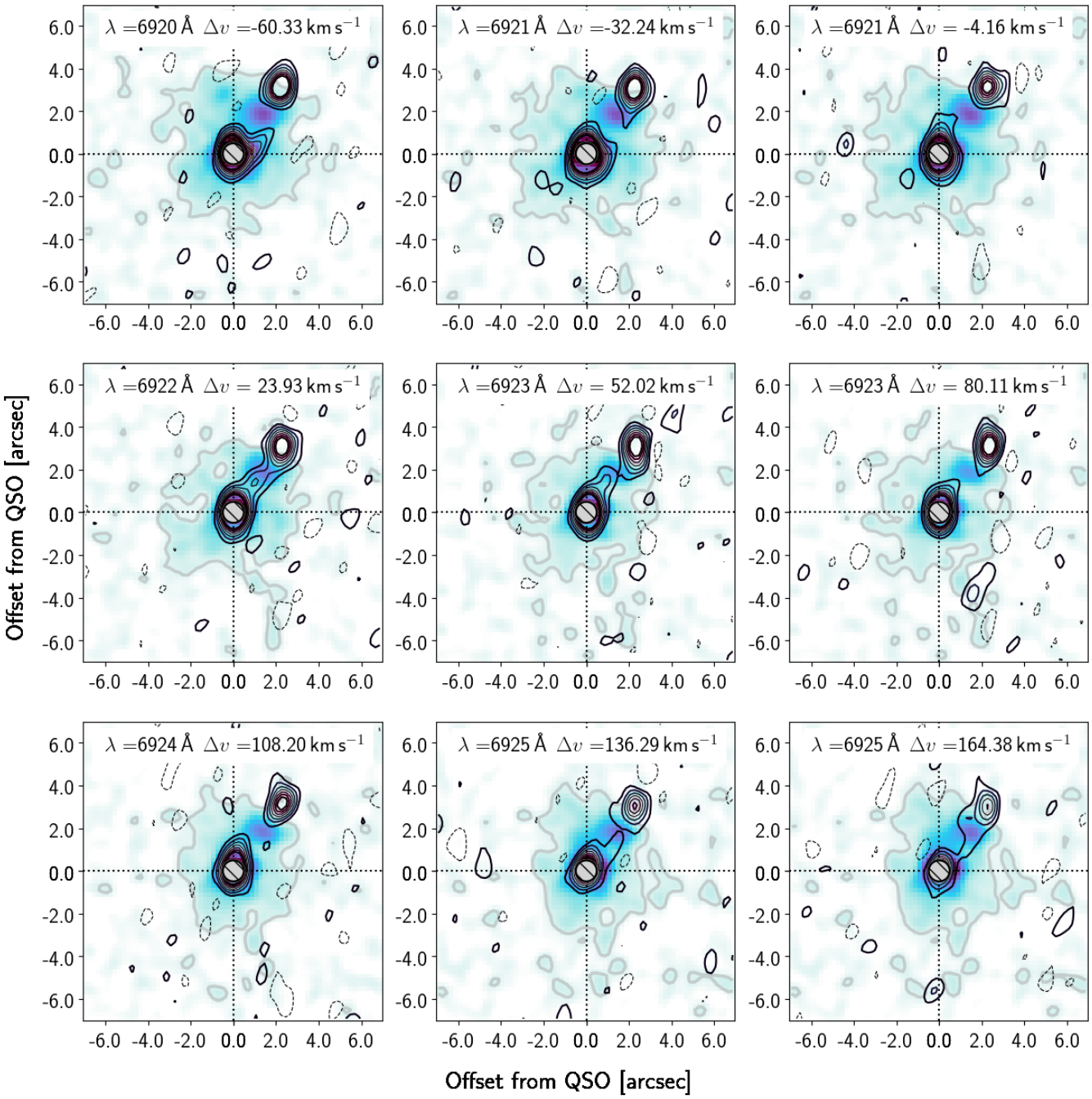

Figure 8. Continued from previous page.

Ouchi, M., Shimasaku, K., Furusawa, H., et al. 2003, ApJ, 582, 60

Overzier, R. A., Guo, Q., Kauffmann, G., et al. 2009, MNRAS, 394, 577

Pavesi, R., Riechers, D. A., Capak, P. L., et al. 2016, ApJ, 832, 151

Petitjean, P., Pécontal, E., Valls-Gabaud, D., & Chariot, S. 1996, Nature, 380, 411

Piqueras, L., Conseil, S., Shepherd, M., et al. 2017, arXiv e-prints, arXiv:1710.03554

Prescott, M. K. M., Momcheva, I., Brammer, G. B., Fynbo, J. P. U., & Møller, P. 2015, ApJ, 802, 32

Rau, U., & Cornwell, T. J. 2011, A&A, 532, A71

Riechers, D. A., Walter, F., Carilli, C. L., et al. 2006, ApJ, 650, 604

Rosdahl, J., & Blaizot, J. 2012, MNRAS, 423, 344

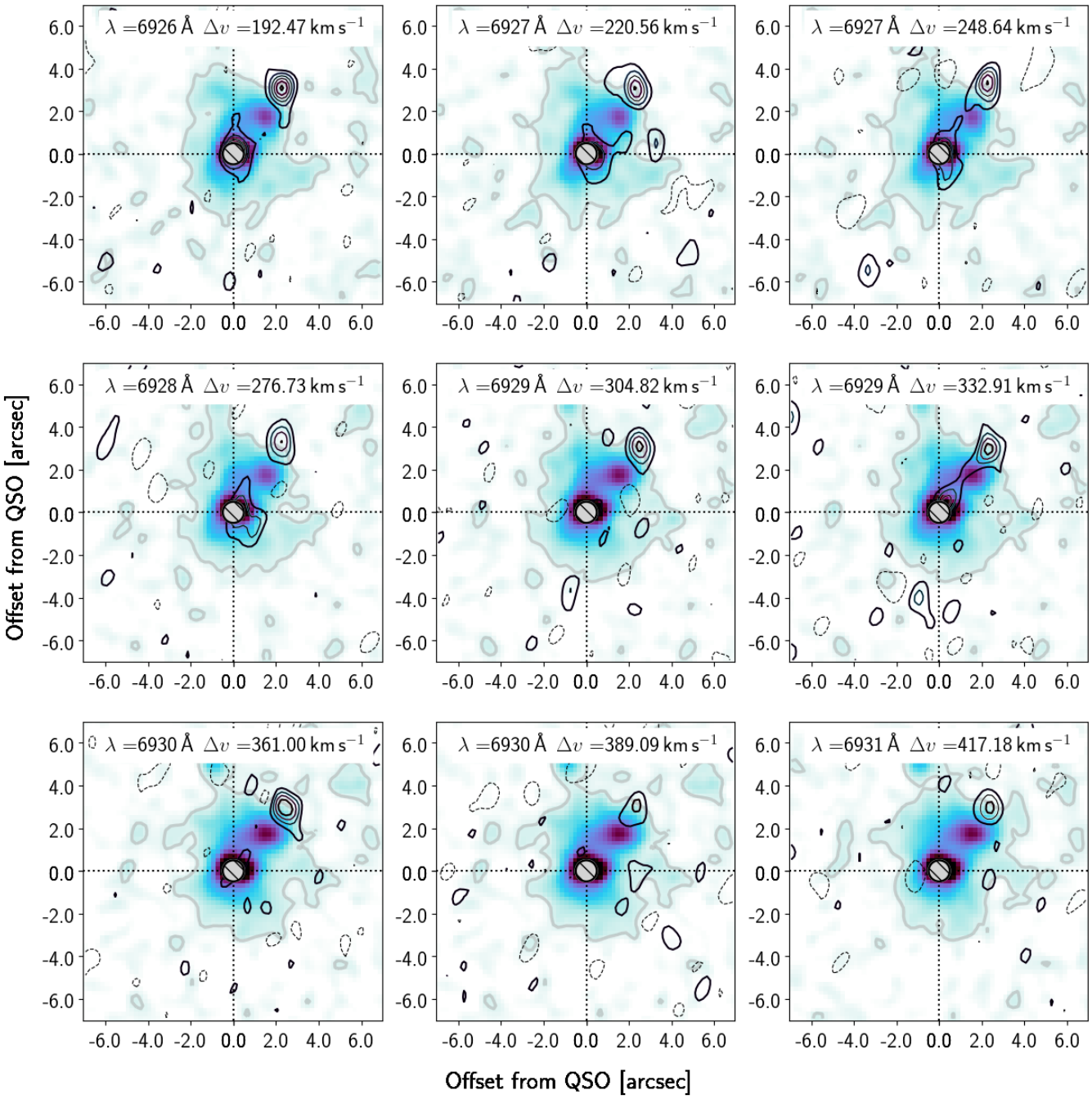

Figure 8. Continued from previous page.

Salomé, P., Guélin, M., Downes, D., et al. 2012, A&A, 545, A57

Schaerer, D. 2003, A&A, 397, 527

Selsing, J., Fynbo, J. P. U., Christensen, L., & Krogager, J. K. 2016, A&A, 585, A87

Smith, D. J. B., & Jarvis, M. J. 2007, MNRAS, 378, L49

Soto, K. T., Lilly, S. J., Bacon, R., Richard, J., & Conseil, S. 2016, Monthly Notices of the Royal Astronomical Society, 458, 3210

Springel, V., Frenk, C. S., & White, S. D. M. 2006, Nature, 440, 1137

Taniguchi, Y., Shioya, Y., & Kakazu, Y. 2001, ApJL, 562, L15

van de Voort, F., Schaye, J., Booth, C. M., Haas, M. R., & Dalla Vecchia, C. 2011, MNRAS, 414, 2458

van Ojik, R., Roettgering, H. J. A., Miley, G. K., & Hunstead, R. W. 1997, A&A, 317, 358

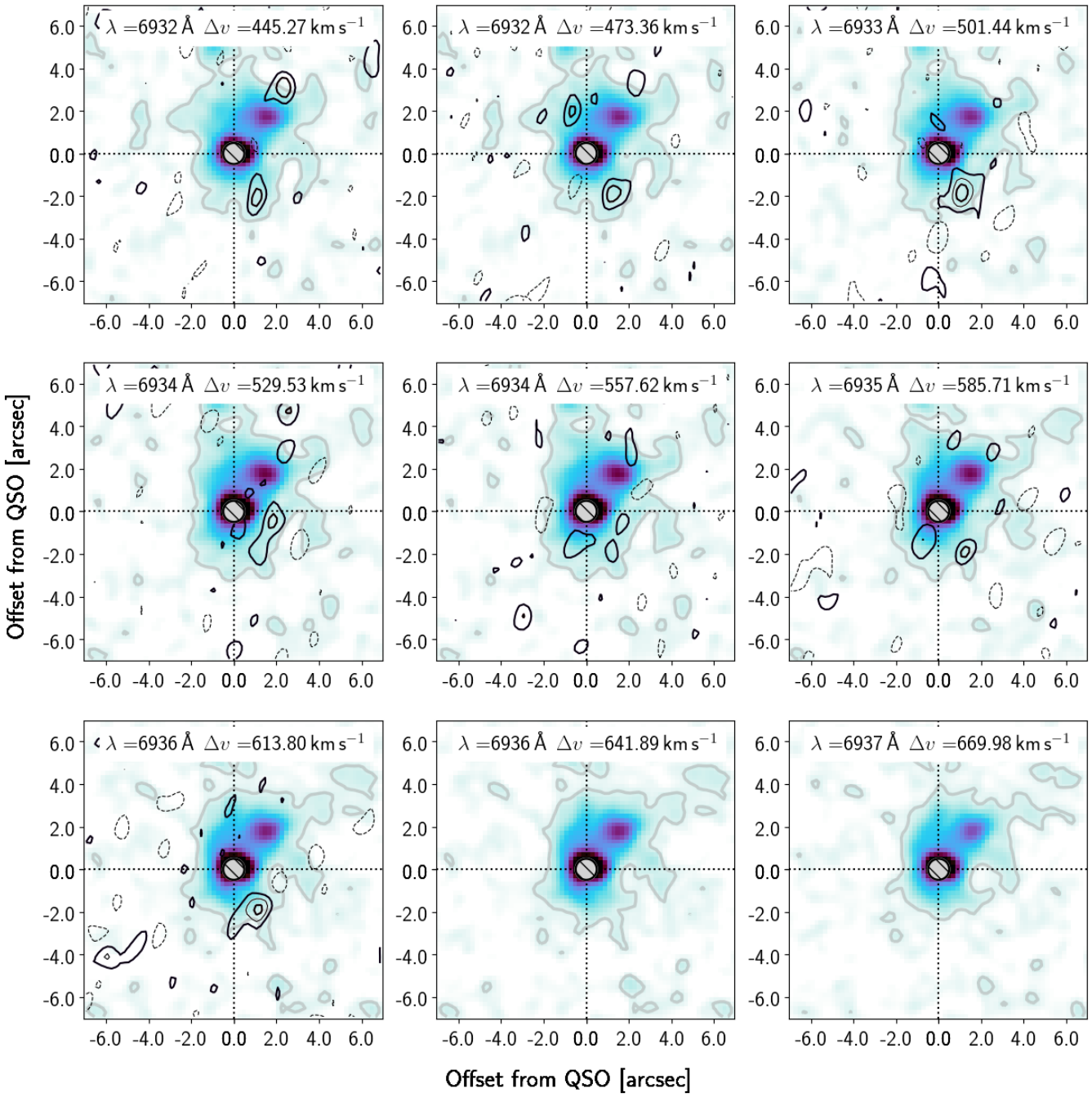

Figure 8. Continued from previous page.

Venemans, B. P., Röttgering, H. J. A., Miley, G. K., et al. 2007, A&A, 461, 823

Wagg, J., Wiklind, T., Carilli, C. L., et al. 2012, ApJL, 752, L30

Weilbacher, P. M., Streicher, O., Urrutia, T., et al. 2012, Society of Photo-Optical Instrumentation Engineers (SPIE) Conference Series, Vol. 8451, Design and capabilities of the MUSE data reduction software and pipeline, 84510B

—. 2014, Astronomical Society of the Pacific Conference Series, Vol. 485, The MUSE Data Reduction Pipeline: Status after Preliminary Acceptance Europe, ed. N. Manset & P. Forshay, 451

Williams, R. J., Wagg, J., Maiolino, R., et al. 2014, MNRAS, 439, 2096

Wisotzki, L., Bacon, R., Blaizot, J., et al. 2016, A&A, 587, A98

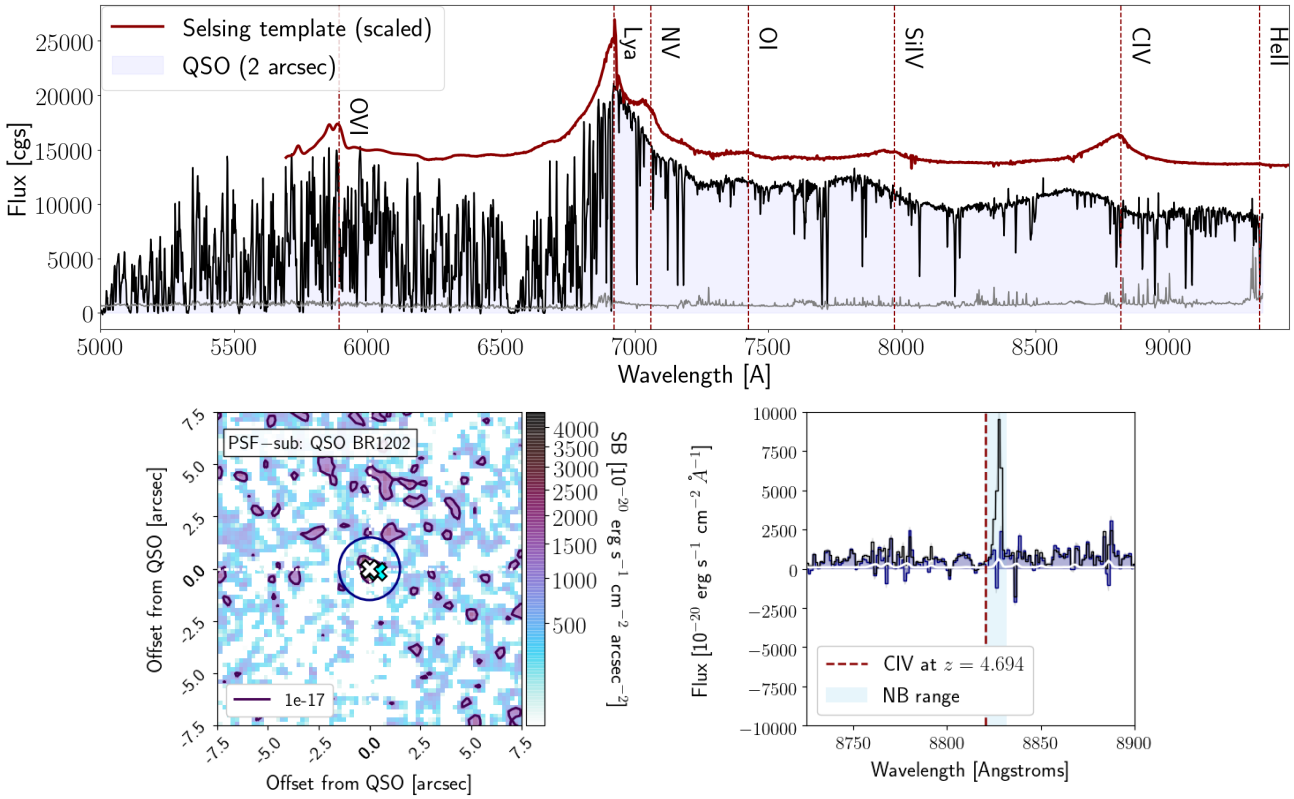

Figure 9. In the top panel we show the QSO spectrum extracted in a two arcsecond diameter aperture (black line, filled blue) and its associated noise (grey). This is overlaid with a QSO template from Selsing et al. (2016) (dark red, offset for clarity) which gives the predicted positions of emission lines in the spectrum. In the lower two panels we show the same two cutouts as in Figure 3, however this time centred on the blue-shifted wavelength region corresponding to CIV emission. No extended CIV emission is detected.

Wootten, A., & Thompson, A. R. 2009, IEEE Proceedings, 97, 1463

Yun, M. S., & Carilli, C. L. 2002, ApJ, 568, 88